

P-type transparent conducting oxides

This content has been downloaded from IOPscience. Please scroll down to see the full text.

2016 J. Phys.: Condens. Matter 28 383002

(<http://iopscience.iop.org/0953-8984/28/38/383002>)

View [the table of contents for this issue](#), or go to the [journal homepage](#) for more

Download details:

IP Address: 128.243.46.132

This content was downloaded on 27/07/2016 at 16:30

Please note that [terms and conditions apply](#).

Topical Review

P-type transparent conducting oxides

Kelvin H L Zhang¹, Kai Xi¹, Mark G Blamire¹ and Russell G Egdell²¹ Department of Materials Science & Metallurgy, University of Cambridge, 27 Charles Babbage Road, Cambridge, CB3 0FS, UK² Department of Chemistry, University of Oxford, Inorganic Chemistry Laboratory, South Parks Road, Oxford OX1 3QR, UKE-mail: kelvinzhanghl@gmail.com

Received 13 May 2016, revised 20 June 2016

Accepted for publication 22 June 2016

Published 27 July 2016

**Abstract**

Transparent conducting oxides constitute a unique class of materials combining properties of electrical conductivity and optical transparency in a single material. They are needed for a wide range of applications including solar cells, flat panel displays, touch screens, light emitting diodes and transparent electronics. Most of the commercially available TCOs are *n*-type, such as Sn doped In₂O₃, Al doped ZnO, and F doped SnO₂. However, the development of efficient *p*-type TCOs remains an outstanding challenge. This challenge is thought to be due to the localized nature of the O 2*p* derived valence band which leads to difficulty in introducing shallow acceptors and large hole effective masses. In 1997 Hosono and co-workers (1997 *Nature* **389** 939) proposed the concept of ‘chemical modulation of the valence band’ to mitigate this problem using hybridization of O 2*p* orbitals with close-shell Cu 3*d*¹⁰ orbitals. This work has sparked tremendous interest in designing *p*-TCO materials together with deep understanding the underlying materials physics. In this article, we will provide a comprehensive review on traditional and recently emergent *p*-TCOs, including Cu⁺-based delafossites, layered oxychalcogenides, *nd*⁶ spinel oxides, Cr³⁺-based oxides (3*d*³) and post-transition metal oxides with lone pair state (*ns*²). We will focus our discussions on the basic materials physics of these materials in terms of electronic structures, doping and defect properties for *p*-type conductivity and optical properties. Device applications based on *p*-TCOs for transparent *p*-*n* junctions will also be briefly discussed.

Keywords: transparent conducting oxide, oxide semiconductor, delafossite, photovoltaics, thin film transistor, cuprous oxide, metal oxide

(Some figures may appear in colour only in the online journal)

1. Introduction to transparent conducting oxides (TCOs)

Electrical conductivity and optical transparency are seemingly mutually exclusive properties when considering conventional solid state materials such as metals, semiconductors and ceramics. Metals are conductive but opaque due to the free electrons at the Fermi level; semiconductors such as Si and GaAs are semi-conducting but showing strong absorption for visible light; ceramics are generally transparent but insulating

due to their large bandgap. Transparent conducting oxides (TCOs) are a class of materials displaying a combination of a close-to ‘metallic’ ($\sim 10^4$ S cm⁻¹) and almost ‘insulating’ transparency (>80%) in the visible light range, achieved by degenerately doping wide bandgap oxide semiconductors. Because of such unique properties, TCOs form the basis of numerous important applications in contemporary and emerging technologies [1–4]. A typical example is the use of TCOs as transparent electrodes for touch screens in smart phones, liquid crystal displays, organic light emitting diodes and solar

cells [3–7]. Emerging technologies include using TCOs as active layers for transparent thin film transistors (TFT) [8–11], UV light emitting diodes and detectors [12], and gas sensors [13–15].

The literature on TCOs is vast, testifying to more than 100 years of intensive scientific investigation and technical application. The first TCO thin film, cadmium oxide (CdO), was made by Badeker in 1907 via thermally oxidizing a vacuum sputtered film of Cd metal [16]. However CdO is not widely used today because of the toxicity issue, whereas it is still of scientific interest because of its high electron mobility [17, 18]. The first large-scale use of TCOs occurred during World War II, when antimony-doped tin oxide (Sb:SnO₂) coating was used as a transparent defroster for aircraft windshields [19]. Electrical heating of windshields and windows in aircraft and vehicles is still an important application of TCOs until now. To date, the industry standard TCOs are *n*-type degenerately doped wide bandgap post-transition metal oxides, including Sn-doped In₂O₃, F-doped SnO₂ and Al-doped ZnO, where the ionic character of the parent oxides produces an oxygen 2*p*-derived valence band (VB) and the metal *s* orbital derived conduction band (CB), resulting in large optical band gaps (>3.1 eV) and concomitantly an excellent *n*-type conductivity when donor doped [20, 21]. Sn-doped In₂O₃ (also called indium-tin-oxide or ITO) accounts for more than 90 percent of the display market, and has been the dominant material for the past 60 years [5]. The materials used in industry are usually in the form of polycrystalline or amorphous thin films deposited on glass or polymer substrates by sputtering techniques. ITO thin films have the advantage of a high conductivity up to $\sim 10^4$ S cm⁻¹, a transmittance of greater than 80% and ease to fabrication. However the low abundance and the ramping price of indium raw metal have significantly increased the cost of ITO in the last two decades. Therefore intensive research efforts from both academia and industry have been devoted to exploiting F-doped SnO₂, Al-doped ZnO, and graphene [22] as possible alternatives to ITO [5, 6].

On the other hand, many potential applications of TCOs are still limited by the lack of their *p*-type counterparts [2, 12, 23, 24]. A high performance *p*-type TCOs would leverage the great promise of oxides for transparent electronics and optoelectronics by combining with the common *n*-type ones into *p*–*n* heterojunctions. The recent rapid development of photovoltaics and solar water splitting also calls for *p*-type electrodes for more efficient hole collection [3]. The challenge in achieving *p*-type TCOs is due to the intrinsic electronic structure of metal oxides: the top of VB of most oxide materials is comprised of strongly localized O 2*p*-derived orbitals [25, 26]. Oxygen is a relatively small atom with a high electronegativity, leading to difficulty in introducing shallow acceptors and large hole effective masses. In 1997, Hosono and co-workers proposed the concept of ‘chemical modulation of the valence band’ (CMVB) to mitigate this problem using hybridization of O 2*p* orbitals with closed-shell Cu 3*d*¹⁰ orbitals [25]. Because the Cu 3*d*¹⁰ level is close to that of an O 2*p*⁶ level, it is expected that the Cu 3*d*¹⁰ can form strong covalent bonding with O 2*p*⁶. This will result in a large dispersion at the

top of VB and reduction of the localization of positive holes. Meanwhile the closed shell *d*¹⁰ also avoids coloration due to *d*–*d* excitations, ensuring the optical transparency for visible light. Following this design rule, a series of *p*-TCOs based on Cu⁺ bearing oxides, such as delafossites CuMO₂ (M = Al [25, 27], Cr [28, 29], In [30], Sc [31], Y [32] and Ga [33]) and SrCu₂O₂ [34] have been discovered. With *p*-type TCO materials identified, the fabrication of a transparent *p*–*n* junction made exclusively from TCO materials became possible [35]. Besides exploring the Cu 3*d*–O 2*p* interaction to enhance VB dispersion, the concept of CMVB was extended to use chalcogens (Ch = S, Se, and Te) to replace the oxygen, since more hybridization between the Cu 3*d* orbitals and the Ch *p* orbitals was expected in the sequence of O, S, Se, and Te. Layered LaCuOCh (Ch = S and Se) [36–39] and Sr₃Cu₂Sc₂O₅S₂ [40] are the two most promising *p*-TCOs identified following this rule. To date Mg-doped LaCuOSe exhibit the highest *p*-type conductivity of 910 S cm⁻¹, but unfortunately the small bandgap of LaCuOSe (2.8 eV) limits its optical transparency [38]. More recently, CMVB has also been applied to other materials with quasi-closed shells such as *d*⁶ and *d*³. This leads to the identification of a series of new *p*-TCOs such as ZnM₂O₄ spinels and Cr-based oxides [41]. Compared to layered Cu⁺-based materials, the new *p*-TCOs normally have 3D lattice structures and are more compatible to integrate with the existing *n*-type materials. Furthermore, cation *s* states are generally more delocalized than *d* states, and their hybridization with O 2*p* states can result in lighter hole effective mass. This can be realized in post-transition metal oxides containing *ns*² lone pair states such as SnO [42] and Ba₂BiTaO₆ [43].

This article aims to provide the readers with an up-to-date review on aforementioned *p*-TCO materials. We will focus our discussions on the basic materials physics of these materials in terms of electronic structures, defect and doping properties for hole conductivity and optical properties.

2. Brief materials physics of TCOs

2.1. Electrical conductivity and electronic structure

The fundamentals of TCOs can be understood by the physics of semiconductors. The electrical conductivity (σ) of a TCO film is directly related to its carrier concentration (*n*) and carrier mobility (μ), according to the relation $\sigma = ne\mu$, where *e* is the elementary charge. These parameters are fundamentally related to the electronic structure of the oxides. The *n* is determined by the intrinsic ease of generation of mobile carriers (electrons for *n*-type and holes for *p*-type) by defects or dopants. The carrier mobility μ is directly proportional to the free carrier scattering time, τ , and is inversely proportional to the carrier effective mass, m^* , via $\mu = e\tau/m^*$. The τ in TCO largely depends on extrinsic factors such as ionized dopants, defects and grain boundaries determined by film preparation procedures. The m^* is an intrinsic property of the materials, a tensor whose components are obtained from the electronic bandstructure by analysing the variation of energy (ε) with momentum (*k*). Thus, a highly dispersive valence band

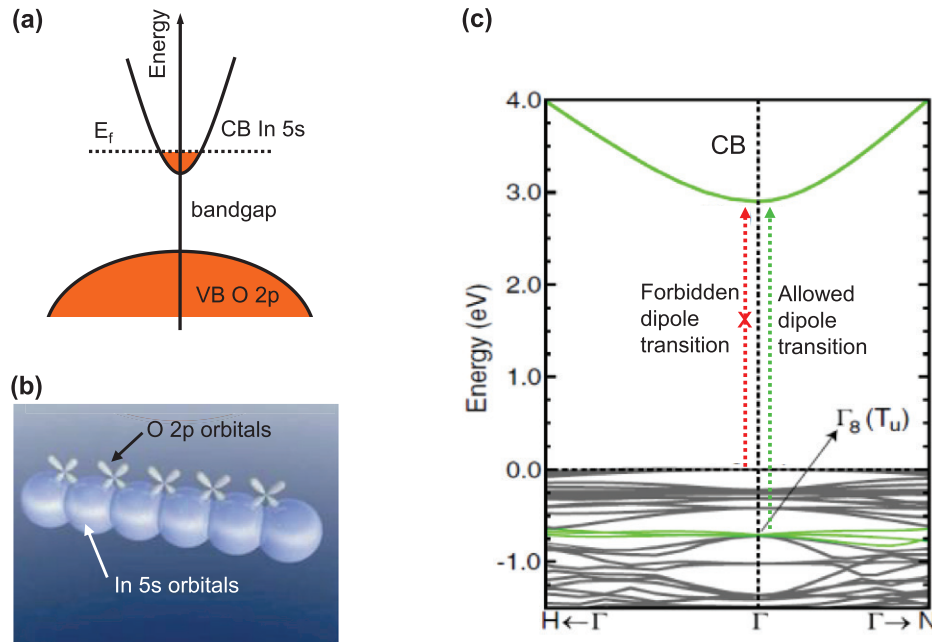


Figure 1. (a) Schematic electronic structure of In_2O_3 doped with Sn, showing the In 5s derived conduction band (CB) and O 2p derived valence band (VB); (b) schematic orbital drawings for In_2O_3 ; large spheres denote In 5s orbitals, showing direct overlap between neighbouring s orbitals; the contribution of oxygen 2p orbitals is small. (Reprinted with permission from Macmillan Publishers Ltd [10], copyright 2004) (c) Density functional theory (DFT) calculated bandstructure of In_2O_3 (Reprinted with permission from [44], copyright 2008 by the American Physical Society).

maximum (VBM) or conduction band minimum (CBM) gives rise to small m^* and hence a high μ .

The design strategy for state-of-the-art TCOs is to degenerately dope wide-bandgap oxide semiconductor to balance the trade-offs between n , m^* and τ . For n -type TCOs, the host materials are post-transition metal oxides (e.g. In_2O_3 , SnO_2 , ZnO and CdO), which usually have a large optical bandgap (>3.1 eV) making the materials highly transparent in the form of thin films. The top of VB is primarily formed by fully filled oxygen 2p⁶ states and the CBM mainly by the unoccupied ns^0 orbitals of post-transition metal cations, as depicted in figure 1(a) for the case of In_2O_3 . The post-transition metal ns^0 derived CBM is the key for achieving a high electrical conductivity in n -type TCOs for the following two reasons. First of all, the ns orbitals of post-transition metal cations normally have large spatial distributions and their wavefunctions overlap with each other (figure 1(b)), which provide a facile pathway for conduction of electrons. In the view of bandstructure, the s orbitals forms a highly dispersive CBM, giving rise to a small electron effective mass. Figure 1(c) plots the bandstructure of In_2O_3 calculated by density functional theory (DFT) by Walsh *et al* [44]. It clearly shows a dispersive CBM at Γ point, while a non-dispersive VBM. In_2O_3 , ZnO and SnO_2 typically have small electron effective masses of 0.20–0.35 m_e (m_e is the rest mass of an electron) and reasonably high electron mobility of 50 cm² V⁻¹ s⁻¹ [5, 20, 45]. On the other hand, the effective masses for hole are as large as 38 m_e for the case of In_2O_3 , suggesting the fundamental limitations to obtaining highly mobile hole at the VBM. This is reflected in part by numerous attempts at p -type doping of ZnO and In_2O_3 [46–48], but no encouraging results have been achieved so far and there are still problems concerning the reproducibility of the results.

Secondly, owing to the d -block contraction, the energy of ns^0 of post-transition metal cations are relatively lower than those of pre-transition metals (e.g. MgO). This gives rise to a relatively high electron affinity and thus ease for doping with electrons [49]. For In_2O_3 , substitution of In^{3+} by Sn^{4+} introduces dopant energy levels just below the CBM. The extra electrons can be easily activated into the CBM as free carriers, inducing a significant increase of conductivity. With more doping, the Fermi level moves up into the CB and the materials ultimately show a degenerately doped semiconductor or a free electron-like metallic behaviour. The critical carrier concentration n_c for the transition from an insulating to metallic phase is defined by the Mott criterion $((n_c)^{1/3} a_0^* > 0.26)$, where a_0^* is Bohr radius. Taking ITO for example, literature suggests that the static dielectric constant $\epsilon(0) = 8.9$, an electron effective mass $m^* = 0.17 m_e$, giving an effective Bohr radius $a_0^* = 2.78$ nm [20]. Thus the n_c for ITO is calculated to be 1×10^{18} cm⁻³. For industry standard ITO, a carrier concentration of 10^{21} cm⁻³ can be achieved, together with a typically electron mobility of 50 cm² V⁻¹ s⁻¹, yielding a high conductivity of 10⁴ S cm⁻¹ [5]. Additionally, it should be noted that Sn dopants in the In_2O_3 lattice behave as point scatters of the itinerant electrons and such scattering events probably set the intrinsic limits for electron mobility.

2.2. Optical properties

The optical properties of the TCO thin films are normally examined by transmittance, reflectance and absorptance spectra in a broad range of UV-visible-infrared spectrum. Their transmittance in the visible and near-infrared regions is a direct consequence of their wide optical bandgaps ($E_g > 3.1$ eV). Here it should be

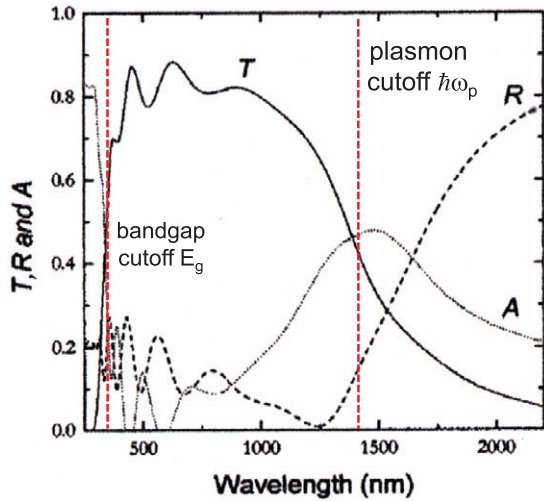


Figure 2. The ‘optical window’ of TCOs set by its plasma edge ($\hbar\omega_p$) at longer wavelengths (lower energy) and optical bandgap at short wavelengths (high energy). (Reprinted from [7], copyright 1981 with permission from Elsevier.)

addressed that the term ‘optical’ bandgap usually means the threshold photon energy showing strong absorption coefficient in optical absorption spectra. The ‘optical’ bandgap is not always equivalent to the fundamental (or electronic) bandgap, because some materials may have a smaller fundamental bandgap that is optically indirect or direct but excitation forbidden. Thereby the materials show very weak absorption at the fundamental bandgap. This point is very evident in the case of In_2O_3 , which has an optical bandgap of 3.6 eV, yet possesses a fundamental but dipole forbidden bandgap of only 2.8 eV, see figure 1(c) [44]. The fundamental bandgap is small because the large In cations lower the antibonding state at the CBM. The optical gap is substantially wider, because optical transitions between the fundamental bandgap are forbidden by the symmetry and the allowed transition is almost 1 eV below the VBM. Similarly most of the Cu^+ -based delafossites *p*-type TCOs have fundamental bandgaps less than 2.8 eV which are indirect and show weak absorptions, but the optical bandgaps are larger than 3.1 eV.

In the near infrared region, the absorption and reflection due to the free carriers in the CB (or VB for *p*-type TCOs) become important. The phenomena in this region can be satisfactorily explained on the basis of classical Drude theory: the free carriers oscillate with an applied field, like the free electrons in metals (plasma oscillations). The plasmon frequency, ω_p given by:

$$\omega_p^2 = \frac{ne^2}{m^*\epsilon(\infty)\epsilon_0}$$

where n is the free carrier density, m^* is the electron effective mass and ϵ_0 is the permittivity of free space. To achieve substantial conductivity, TCOs often require carrier concentrations on the order of $1 \times 10^{21} \text{ cm}^{-3}$, which results in a plasmon energy in the near-infrared region at around 0.9 eV. However a higher electron concentration of $5 \times 10^{21} \text{ cm}^{-3}$ will bring the plasmon energy into the visible red spectral range. Thus the plasmon frequency for free carriers place a limit on the

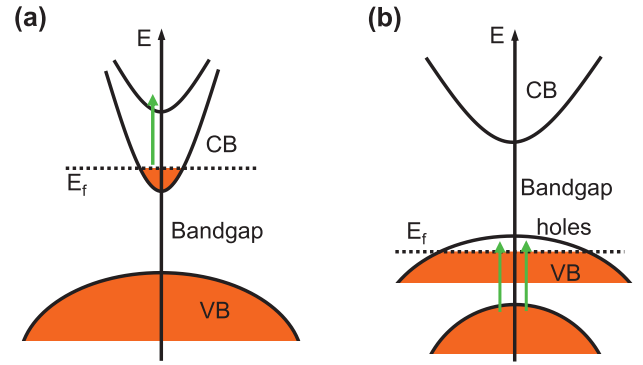


Figure 3. New transitions in highly doped TCOs, as marked by green arrows; (a) for *n*-TCOs, electronic transitions from CB to higher energy states, (b) for *p*-TCOs, electronic transitions from lower energy states to the hole state created at the top of VB.

optimum region of transparency associated with a particular conductivity. Therefore the ‘transparent window’ for typical TCOs is set at short wavelengths by its optical bandgap and at longer wavelengths by its reflectivity plasmon edge ($\hbar\omega_p$). Figure 2 shows transmission and reflection spectra from ultra-violet to near infrared wavelengths of an ITO films [7]. Loss in transmission at high and low wavelengths is ascribed to free carrier absorption and interband excitations.

Moreover, the additional high concentration of electrons or holes inserted into the CB (for *n*-type) or the VB (for *p*-type) can also lead to new optical transitions. As schematically shown in figure 3(a), the electrons in the CB can absorb photons and undergo transitions to higher states. Likewise, in *p*-type TCOs (figure 3(b)), the electrons in lower states can transition up and recombine with the holes in the VB. Such second gap transitions may affect significantly the transparency of TCOs.

2.3. Figure of merits (FoM)

It is obvious that the selection criteria for a high-performance TCO are of high conductivity and high transparency. From a practical point of view, these materials should also be cheap to produce, and preferably non-toxic. Researchers have been searching for a standard criterion, FoM, to assess the performance of materials. In 1976, Haacke [50] proposed a simple and useful FoM that correlate the transmittance (T) and the sheet resistance R_s (where $R_s = 1/\sigma d$, d is the film thickness) by,

$$\text{FoM} = T^q/R_s = T^q\sigma d$$

where q is an exponent that determines which transmittance is required for a specific purpose. $q = 10$ is chosen because a transmittance of 90% is sufficient for most purposes. However this quantification overweighs the importance of optical transparency. A material could have a high FoM for a transmittance $>90\%$, even though the sheet resistance is very high (recall the q exponent). One in principle can artificially make a material with high FoM by just making it thin enough.

The second approach with improvement proposed by Gordon [51] was to use the ratio σ/α , where α is the visible

Table 1. A brief summary of major *p*-type TCOs reported in the literature.

Materials	Structure	Growth methods	<i>d</i> (nm)	<i>T</i> (%)	<i>E</i> _{opt} (eV)	σ (S cm ⁻¹)	<i>n</i> (cm ⁻³)	μ (cm ² V ⁻¹ s ⁻¹)	FoM ^H	FoM ^G	Ref.
Sn:In ₂ O ₃ (ITO)	Bixbyite	Sputtering	115	85	3.7	5900	1.2×10^{21}	30	13 300	4×10^6	
Cu ₂ O	Cubic	PLD	650	—	2.17	0.014	1.7×10^{14}	90	—	—	[63]
CuBO ₂	Delafossite	PLD	200	75	4.5	1.65	1×10^{17}	100	1.8	115	[99]
CuAlO ₂	Delafossite	PLD	500	28	3.5	0.95	1.3×10^{17}	10.4	0.0002	37	[25]
CuAlO ₂	Delafossite	PLD	230	70	3.5	0.34	2.7×10^{19}	0.13	0.22	21	[27]
CuCr _{0.95} Mg _{0.05} O ₂	Delafossite	Sputtering	250	30	3.1	220	—	—	0.03	4570	[28]
CuGaO ₂	Delafossite	PLD	300	80	3.6	0.02	1.7×10^{18}	0.23	0.2	8.4	[33]
CuScO _{2+x}	Delafossite	Sputtering	110	40	3.7	15	—	—	0.02	180	[31]
CuIn _{0.93} Ca _{0.03} O ₂	Delafossite	PLD	100	40	3.7	0.006	—	—	0.001	0.14	[30]
CuY _{1-x} Ca _x O ₂	Delafossite	Sputtering	100	41	3.5	1	—	—	0.003	27	[32]
SrCu ₂ O ₂	Tetragonal	PLD	120	80	3.3	0.048	—	—	0.6	2.6	[34]
La _{0.97} Sr _{0.03} CuOS	Tetragonal	Sputtering	150	60	3.1	20	—	—	1.8	587	[137]
La _{0.8} Mg _{0.2} CuOSe	Tetragonal	Sputtering	40	—	2.8	910	1.7×10^{21}	3.5	—	—	[144]
ZnRh ₂ O ₄	Spinel	PLD	100–300	55	2.74	2.75	—	—	0.13	91	[41]
ZnIr ₂ O ₄	Spinel	PLD	100–300	61	2.97	3.39	—	—	0.47	136	[41]
Mg _x Cr _{2-x} O ₃	Corundum	Solution	150	65	3.3	0.33	—	—	0.07	11	[163]
La _{0.75} Sr _{0.25} CrO ₃	Perovskite	MBE	80	55	4.6	15	3.4×10^{21}	0.03	0.26	196	[164]
La _{0.50} Sr _{0.50} CrO ₃	Perovskite	MBE	50	43	4.6	56	7.5×10^{21}	0.04	0.05	326	[164]
SnO	Litharge	PLD	20	—	2.8	0.1	2.5×10^{17}	2.4	—	—	[42]
SnO	Litharge	Sputtering	200	0.85	2.8	0.77	1×10^{18}	4.8	3	95	[178]
Ba ₂ BiTaO ₆	Perovskite	PLD	120	90	4.5	0.005	1×10^{14}	30	0.02	0.57	[43]
Li:NiO	Rocksalt	Sputtering	118	30	3.4	7.1	—	—	0.0005	70	[185]

PLD: pulsed laser deposition; *d*: film thickness; *T*: transmittance in visible range; *E*_{opt}: optical bandgaps; σ : conductivity; *n*: carrier concentration; (some of the values are calculated by the authors according to $\sigma = ne\mu$); μ : hall mobility; FoM^H: figure of merit by Haackle; and FoM^G: figure of merits by Gordon. The parameters for ITO are typical value for commercialized substrates.

absorption coefficient. The α is calculated from the total visible transmission and corrected for reflectance (or sometime neglecting reflectance). In the neglecting reflectance approximation, $\alpha \approx (1/d) \ln(1/T)$ and FoM $\approx -1/(R_s \ln T)$ (in units of M Ω^{-1}). The advantage of this approach is the FoM does not depend on the thickness of the films, which allows more intrinsic performance of the materials to be assessed. However the functional form of this FoM means that the actual numerical values are strongly affected by changes in R_s , and are less affected by changes in *T*. This method seems to yield very high values for highly conductive samples, even when the optical transparency is low. For example, as shown in the following, the Cu_xCr_{1-x}Mg_xO₂ film is doped sufficiently high that σ is 220 S cm⁻¹, and *T* is 30% [28]. The FoM for this film is 4600 M Ω^{-1} , the highest values of all *p*-TCOs reported. However the 30% transmittance would exclude the material a good TCO. Thus, while the FoM is a convenient parameter for the comparison of different materials from different groups, it should not be presented in isolation. It is important to look beyond the FoM and also consider σ , *T*, and *d* when evaluating *p*-type TCOs.

In table 1, we summarize these parameters of the representative *p*-type TCOs in the literature. Both FoMs by Haacke (FoM^H) and Gordon (FoM^G) are also calculated for the readers' reference. In figure 4, we also plot the transmission versus inverse sheet resistance (equivalent to sheet conductance) of these *p*-type TCOs (red squares) and commercial *n*-type ITO,

which provide a direct overview on the performance of *p*-type TCOs so far. There is still a huge gap towards the comparable performance with commercial *n*-type ITO.

2.4. Design rules for *p*-type TCOs

Lessons from *n*-type TCOs point out it is intrinsically a difficult task to obtain a high *p*-type conductivity. This is caused by (i) the localized nature of O 2*p* orbitals at the VBM (limiting the hole mobility); and (ii) the difficulty in *p*-type doping of most oxides (limiting the carrier concentration *n*)—in simple chemical terms, *p*-type doping involves the introduction of holes into the O 2*p* states at VBM (i.e. oxidation of oxide ions); this results in strongly localized, deep lying holes centered on single oxygen sites. The key to alleviate this issue is to design a material with cations that introduce occupied cation *d* or *s* states near the VBM. The resulting *p*-*d* and *p*-*s* coupling enhances cation-O 2*p* hybridization and increase the dispersion at VBM for a low effective mass. In the following we list the design principles for *p*-type TCOs as suggested in literature [52–55]:

2.4.1. Transparency. The optical bandgap must be larger than 3.1 eV to guarantee transparency to the visible light. Note also that the intraband absorption from deeper VB states to the hole states should be weak or not in the visible light spectrum so as not to curtail transparency.

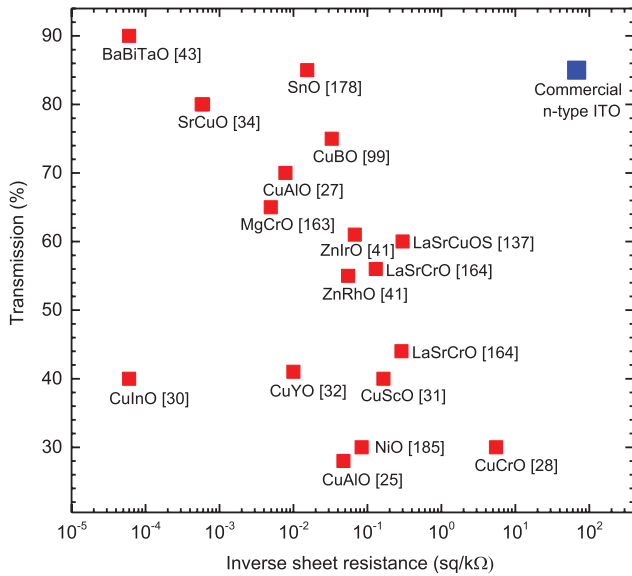


Figure 4. Graphical summary of optical transmission and inverse sheet resistance of the representative *p*-type TCOs in the literature (red squares) and commercial *n*-type ITO. The numbers in brackets are the reference.

2.4.2. Hole carrier concentration. Hole-producing defects (i.e. acceptors) should have low formation energies, making them easy to form either as intrinsic acceptors or as extrinsic dopants soluble in the host compounds. The energy levels of the acceptors should be shallow enough so that free hole carrier can be easily activated at the VBM. ‘Hole-killing’ defects, such as oxygen vacancies, should be difficult to form. A review of defect formation energies of transparent oxides by Robertson and Clark summarized the following criteria for doping [55]: for *n*-type doping a large electron affinity (χ , energy between the vacuum level and CBM) is necessary, while for *p*-type doping a small ionization potential (IP, energy difference between the vacuum level and the VBM) is required.

In the following sections, we will discuss each criterion of *p*-type TCOs reported in the literature based on these design rules.

3. Cu⁺-based materials (3d¹⁰)

3.1. Cu₂O

It is illustrative to start with Cu₂O because it is a prototype *p*-type metal oxide, showing a hall mobility exceeding 100 cm² V⁻¹ s⁻¹. Although its small bandgap (2.17 eV) precludes it as a *p*-type TCO, its electronic structure form the basic concept for designing high mobility *p*-type oxides. Cu₂O has a cubic crystal structure (space group $pn\bar{3}m$, $a = 4.27$ Å) [56]. It consists of a body centered array of oxygen ions (see figure 5(a)) with Cu ions occupying half the sites between adjacent oxygen ions, in such a way that each oxygen ion is surrounded by a tetrahedron of Cu ions and each Cu is linearly coordinated by two oxygen ions forming O–Cu–O dumbbell units. The structure can

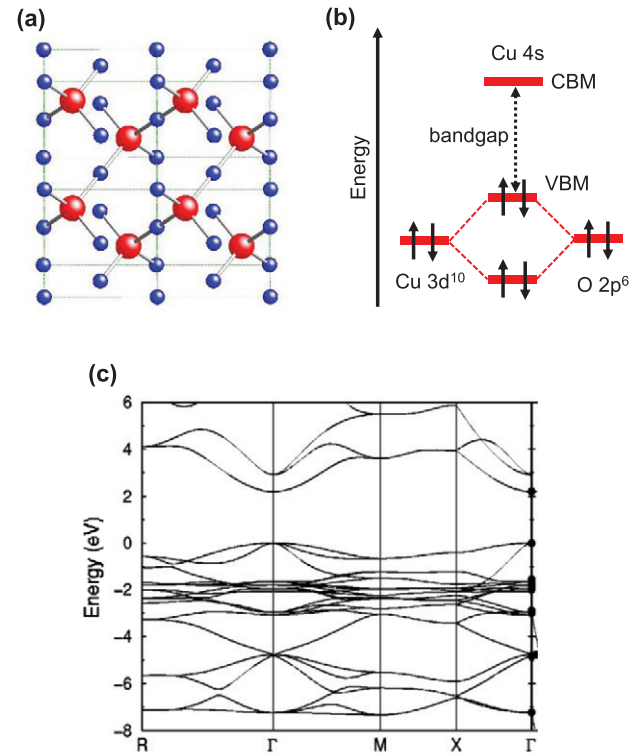


Figure 5. (a) Crystal structure of Cu₂O; large red balls denote oxygen and small blue balls for Cu; (b) schematic energy diagram showing the hybridization of O 2p with Cu 3d; (c) LDA calculated bandstructure of Cu₂O by Nie *et al.* (Reprinted with permission from [83]. Copyright 2002 by the American Physical Society.)

alternatively be described in terms of two interpenetrating anti-SiO₂ cristabolite nets. The separation between adjacent Cu ions in the two different nets is relatively small (3.02 Å) compared with that found in metallic copper (2.56 Å). The short Cu–Cu distance can still allow significant 3d¹⁰–3d¹⁰ interactions, which was thought to be the cause of the small bandgap of Cu₂O [57, 58].

Cu₂O have been widely explored as one of the most promising materials for solar cells since the 1920s due to their high solar spectral absorption coefficient, high mobility, low-cost, and nontoxicity [59–61]. Furthermore, due to the high *p*-type mobility, its applications in oxide TFT were also extensively explored by researchers [11, 62–64]. The preparation of Cu₂O thin films has been reported using a variety of growth techniques, such as pulsed laser deposition (PLD) [63, 65, 66], magnetron sputtering [64, 67–70], thermal oxidation [71, 72], spin coating [73, 74], atomic-layer deposition [75], chemical vapor deposition [76], and so on. Among all these methods, sputtering is a relatively cost effective and the most conventional method that can be used for large area deposition of polycrystalline films, while PLD is usually used to grow epitaxial thin films on single crystal substrates [63, 65]. The obtained Hall mobilities varied largely from 0.1 to 256 cm² V⁻¹ s⁻¹. Li *et al* achieved a record mobility of 256 cm² V⁻¹ s⁻¹ in Cu₂O polycrystalline thin films by introducing a low-temperature buffer Cu₂O layer to control the preferential crystalline orientation and increase the grain size [67]. An increasing Hall mobility was found with larger grain sizes,

indicating that grain-boundary scattering is a major contributor in limiting the electrical properties. Matsuzaki and co-workers have grown Cu_2O epitaxial thin films on both $\text{MgO}(001)$ and (110) substrates and their films possess a hole mobility of up to $90\text{ cm}^2\text{ V}^{-1}\text{ s}^{-1}$ at room temperatures [63]. Interestingly, the hole mobility increased up to $\mu = 363\text{ cm}^2\text{ V}^{-1}\text{ s}^{-1}$ as temperature decreased to 170 K. The authors also fabricated p -channel TFT using the Cu_2O films. However the device only exhibited a low field-effect mobility at $0.26\text{ cm}^2\text{ V}^{-1}\text{ s}^{-1}$, regardless of the high phase purity and Hall mobility of the thin films they achieved. This result implied possible extra trap states at the channel and/or channel-gate interface produced during device fabrication process, e.g. by ion bombardment and/or plasma reduction, may play an important role in determining the device performance [77]. This is also true for application of Cu_2O in solar cells. It has been demonstrated that the formation of interfacial defect states (possibly CuO) between the heterojunction of p - Cu_2O and n - ZnO is detrimental to the efficiency of Cu_2O -based solar cells [78–80]. Therefore controlling the surface and interface chemistry of Cu_2O thin films with other materials might be the solution to address the problem.

The higher p -type mobility of Cu_2O is related to the nature of the bandstructure near the top of VB. The VB of most metal oxides are mainly composed of O $2p$ orbitals, meaning that p -type doping often results in localized holes deep in the bandgap. In contrast, Cu^+ in Cu_2O has $3d^{10}$ close shell electronic configuration. The energy level of Cu $3d^{10}$ is close to that of O $2p^6$ orbitals (figure 5(b)). This leads to a considerable covalency between the two orbitals. In such a way, a more dispersed VBM with a smaller hole effective mass can be achieved. Photoelectron spectroscopy measurements and bandstructure calculations clearly show that the Cu $3d$ levels and the O $2p$ states are close in energy and that these form the top of VB [81, 82]. Figure 5(c) shows the bandstructure of Cu_2O calculated by Nie *et al* using DFT-local density approximation (LDA) [83]. It clearly shows that the VBM at Γ point is much more dispersive than that of In_2O_3 (figure 1(c)). By analysing the variation of energy (ϵ) with momentum (k), the authors also report a hole effective mass as low as $0.24 m_e$. This value is slightly smaller than the experimental data ($0.58 m_e$ and $0.69 m_e$) measured by cyclotron resonance [84], due to the underestimation of the bandgap by LDA. DFT has a well-known tendency to underestimate bandgaps in most semiconductors and insulators; this tendency is due mainly to a discontinuity in the exchange correlation potential. Nonetheless, these results provide a microscopic mechanism for the p -type high mobility found in Cu_2O .

It is now widely accepted that the source of p -type carriers in Cu_2O is Cu vacancies (V_{Cu}), via, $V_{\text{Cu}} \rightarrow \text{Cu}^{(0)} + \text{h}^*$ (the formation of a V_{Cu} is associated with removal of one Cu atom from the lattice, together with one hole state above the VBM) [85–87]. This is supported by accumulative experimental observations that the hole concentration in Cu_2O are strongly correlated with oxygen partial pressure during growth or post-growth annealing conditions in oxygen [56, 67]. A direct evidence of V_{Cu} has been reported by Ameena *et al* by using positron annihilation spectroscopy (PALS) in conjunction

with Doppler broadening spectroscopy (DBS) and photoluminescence (PL) spectroscopy [88]. Theoretical studies based on different methods (LDA, GGA + U) also consistently predicted V_{Cu} has the lowest formation energy compared to the other possible defects (e.g. oxygen interstitial) both under Cu-poor-O-rich condition, and under Cu-rich-O-poor condition [83, 86, 89, 90].

What is unclear is on the energy level of the hole state (i.e. the acceptor level). The hole states have been reported in experiments in the range of 0.12–0.70 eV above the VBM [65, 90–93]. Based on the elementary effective mass theory, the acceptor energy can be roughly estimated by $E_A = 13.6 m^*/m_0 \epsilon_r^2$, giving a hole energy level of 0.156 eV above VBM. This is of course an oversimplified estimation, because unlike conventional semiconductors with covalent bonding, Cu_2O is an ionic compound in which the charge carrier favours the formation of self-trapped polarons by distorting the surrounding lattice [90]. The polaronic nature of the carrier would result in much deeper acceptor levels trapped in the bandgap. Deep acceptor states were observed with photoinduced current transient spectroscopy, with the defect states having activation energies ranging from 0.12 to 0.63 eV above the VBM [91]. The acceptor state at 0.63 eV was assigned as V_{Cu} acceptor-type state but none of the other defect levels were assigned. Paul *et al* recently performed a detailed study on the defects of Cu_2O using deep level transient spectroscopy with a broad temperature range of 100 to 350 K, and reported two hole trap levels [92, 93]. The first at 0.45 eV above the VBM, similar to the ones found by others [91], was attributed to V_{Cu} , while the second level located at 0.25 eV was tentatively assigned to a Cu di-vacancy. Scanlon and Watson *et al* have calculated the energetics and the transition levels of acceptor defects in Cu_2O using the hybrid-DFT approach [86, 90]. They successfully predicted the two transition levels, one at 0.47 eV and the other at 0.22 eV, in excellent agreement with the DLTS study by Paul *et al* and others [92, 93]. Their results were also consistent with the polaron hopping transport mechanism as experimentally observed Arrhenius-like temperature dependence conductivity [64, 94].

3.2. Delafossite (CuMO_2)

3.2.1. Crystal structures and thin film growth. For all reported Cu_2O thin films, despite the encouraging hall mobility values, a major concern is the low carrier concentration ($\sim 10^{14}\text{ cm}^{-3}$) and low optical bandgap (ca. 2.17 eV), which limit the potential of Cu_2O thin films in fully transparent electronics. The small bandgap of Cu_2O was believed to be due to the strong Cu–Cu interaction in a cuprite structure: each Cu ion has 12 next-nearest Cu^+ neighbours [27, 58]. It was therefore suggested that a large bandgap might be found in ternary Cu^+ . Hosono and co-workers found thin films of CuAlO_2 have a large optical bandgap of 3.5 eV and therefore show simultaneously an optical transparency of 70% and p -type conductivity of 1 S cm^{-1} [25]. Figure 6 shows the optical transmission spectra and temperature dependent conductivity measurement of CuAlO_2 thin film, originally reported in [27]. This pioneering work has aroused intense interest for search for

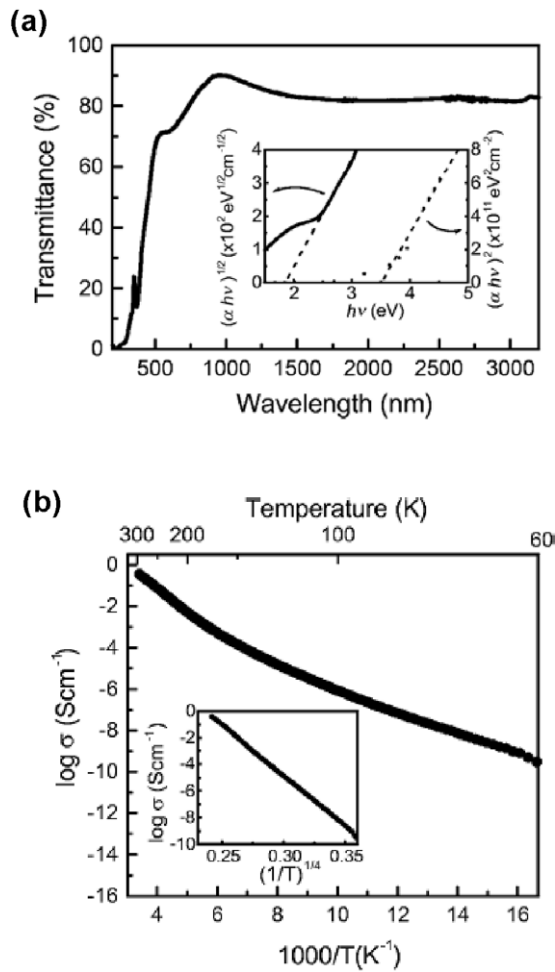


Figure 6. (a) Optical transmission spectrum of CuAlO₂ thin film (the film thickness is 230 nm). The inset shows the plots of $(\alpha h\nu)^{1/2}$ versus $h\nu$ and $(\alpha h\nu)^2$ versus $h\nu$ for estimation of indirect and direct bandgap of CuAlO₂. (b) Arrhenius plots of electrical conductivity of CuAlO₂ thin film as function of temperature. (Reprinted from [27] with the permission of AIP Publishing.)

other Cu⁺-based delafossites with the general chemical formula CuMO₂ in which M is a trivalent cation such as B, Al, Cr, Ga, Sc, In or Y. In the delafossite structure (figure 7(a)), each Cu atom is linearly coordinated with two oxygen atoms, forming O–Cu–O dumbbells parallel to the *c* axis. The oxygen anions in the O–Cu–O dumbbells are also each coordinated to three M³⁺ cations, oriented such that the M-centered octahedral form MO₂ layers which lie parallel to the *ab* plane. The O–Cu–O dumbbell and the octahedral MO₂ can be arranged in layers so that a stacking sequence of *ABABAB* gives the 2H (*P63/mmc*) hexagonal polymorph or *ABCABC* gives the 3R (*R3m*) rhombohedral polymorph.

Table 2 summarizes the structural parameters of the undoped CuMO₂ (*R3m*) which were retrieved mostly from powder ceramics prepared by solid state synthesis back in the 1980s [95–97]. It can be seen that the lattice parameters and bond lengths follow well the trend of ionic radius of M³⁺. The local coordination around Cu⁺ in CuMO₂ is very similar to that in Cu₂O, i.e. the same O–Cu–O dumbbells and similar Cu–O bond distance. The most important difference between the two oxides is that the O–Cu–O units in Cu₂O are connected

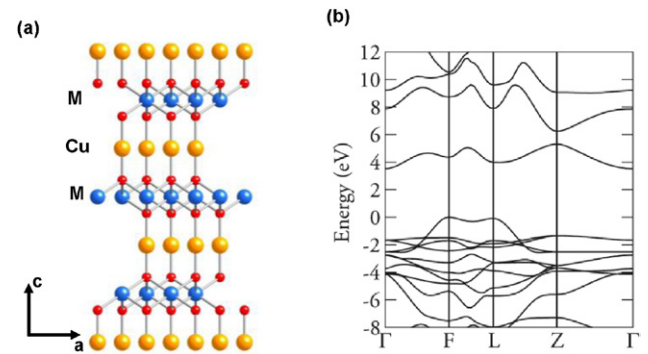


Figure 7. (a) Crystal structure of CuMO₂; (b) HSE06 calculated bandstructure of CuAlO₂, plotted with reference to the top of the VB (0 eV); it clearly shows the dispersion of VBM at F- and L-point. The CBM is found at the Γ -point, making it an indirect bandgap material. Calculation also show the VBM is derived from hybridized Cu 3*d* and O 2*p* orbitals, while the CBM is a mixture of Cu 4*s* and 3*d* with O 2*p* orbitals. (Reprinted with permission from [113]. Copyright 2010 American Chemical Society.)

in three dimensions, whereas in CuMO₂ the O–Cu–O units are isolated by the MO₂ layers into two-dimension sheet. Therefore the number of next-nearest-neighbours is reduced from 12 in Cu₂O to 6 in CuMO₂. It has been argued that the reduced dimensionality of the Cu–Cu interactions is of central importance in determining that the bandgap of CuAlO₂ (originally quoted as 3.5 eV) is wider than that in Cu₂O (2.17 eV) [25, 27]. However, there is an oversimplified picture, because one should note that the Cu–Cu bond distance in CuMO₂ (2.86 Å) is shorter than that of Cu₂O (3.02 Å) [58, 98].

Since the seminal work of CuAlO₂, considerable effort has been made to grow a variety of CuMO₂ (M = B [99, 100], Al [25, 27], Cr [28], Ga [33], Sc [31, 101], In [30, 102] and Y [32]) and their alio-valent cation doped thin films (e.g. Mg doped CuCrO₂, Mg doped CuAlO₂) by techniques such as PLD [25, 27, 30, 33, 101], sputtering [28, 31, 32, 102, 103], molecular beam epitaxy [104], chemical solution methods [105–107], and so on (see [24] for a comprehensive review on the *p*-type TCO deposited by different techniques). PLD is the most popular growth method because it has the advantage of growing high-quality epitaxial thin films with well-controlled compositions and morphology. The epitaxial growth of CuMO₂ film with reduced defects and grain boundaries would be desirable for (opto-)electronic device application (e.g. transparent *p*–*n* diodes) as well as for fundamental research to study the intrinsic properties of the materials. However preparing a high-quality CuMO₂ ceramic target is challenging because of the metastable oxidation state of Cu⁺ and the ease to form secondary phase [108]. Basal plane alumina Al₂O₃(0001) was the most popular substrate for attempted epitaxial growth of CuMO₂ films, and silica substrate were also used for polycrystalline films. The structure of alumina belongs to the rhombohedral space group *R3c*. It is based on a hexagonally close packed array of oxygen ions with occupation of 2/3 of the octahedral holes between successive layers by aluminium ions. The average O–O separation in the close packed layers is $d_{O-O} = a_{Al_2O_3}/\sqrt{3} = 2.748 \text{ Å}$.

Table 2. Structural data, nearest-neighbor interatomic distances, bandgaps and calculated effective masses for the CuMO_2 and Cu_2O ; the numbers in brackets are the reference.

	Cu_2O [58, 83]	CuBO_2 [99, 116]	CuAlO_2 [111, 113]	CuCrO_2 [104, 115]	CuGaO_2 [33]	CuScO_2 [31, 115]	CuInO_2 [104, 115]	CuYO_2 [32, 115]
a (Å)	4.435	2.84	2.858	2.97	2.980	3.24	3.292	3.53
c (Å)	—	16.52	16.96	17.10	17.10	17.13	17.39	17.14
M^{3+} size (Å)	—	0.41	0.67	0.75	0.76	0.88	0.94	1.04
Cu-O (Å)	1.85	—	1.86	1.84	1.85	1.83	1.84	1.82
M-O (Å)	—	—	1.91	2.03	1.99	2.12	2.17	2.28
Cu-Cu (Å)	3.02	2.85	2.858	2.97	2.98	3.24	3.292	3.53
Direct E_g	2.17	4.5	3.47	3.1	3.6	3.3	3.9	3.5
Indirect E_g	—	2.2	2.97	2.5–2.6	NA ^a	NA ^a	NA ^a	NA ^a
m^* [001]	0.24	1.71	38.95	6.07	NA	8.22	NA	7.64
m^* [010]	0.24	0.45	2.6	4.53	NA	4.00	NA	3.72

^a CuGaO_2 , CuScO_2 , CuInO_2 , and CuYO_2 all have indirect bandgap according to DFT calculations ([120]) and experimental optical transmission data. However there are no exact values reported so far.

Note: The lattice parameters and interatomic distances are gathered from [95–97].

It is thus expected the CuMO_2 can be epitaxially grown on the $\text{Al}_2\text{O}_3(0001)$ by matching of both the crystal symmetry and the nearest-neighbour O–O distances. For example, the in-plane lattice parameter and also the $d_{\text{O-O}}$ of CuAlO_2 are 2.858 Å; and thus the mismatch between CuAlO_2 and Al_2O_3 can be defined by $f = (2.858 - 2.748)/2.748 = 4.0\%$, with CuAlO_2 under compressive strain. It has been shown that the c axis of CuAlO_2 is parallel to that of Al_2O_3 substrate, and the in-plane axes rotate 60° around the c axis to keep the close-packed stack of oxygen ions at the interface of between CuAlO_2 and Al_2O_3 [109]. Similar epitaxial relationships have been observed for CuBO_2 [99], CuCrO_2 [104] and CuGaO_2 [33, 107]. However, with the increase of the ionic size of M cations, the lattice mismatch is too large to maintain the epitaxial relationship (e.g. $f = 19.8\%$ for the case of CuInO_2). Yanagi *et al* found the growth of Ca- and Sn- doped CuInO_2 on $\text{Al}_2\text{O}_3(001)$ leads to polycrystalline films [30].

3.2.2. Electronic and optical properties. The optical and electrical properties of the films were commonly evaluated by UV-visible absorption, temperature dependent conductivity measurement, Hall and Seebeck coefficient measurement, and the results are summarized in table 1 and figure 4. Compared to Cu_2O , Cu-based delafossites normally have higher conductivity and transparency, but lower hole mobility ($< 10.4 \text{ cm}^2 \text{ V}^{-1} \text{ s}^{-1}$). Sleight and co-workers suggested the lower mobility in the p -type delafossites may be due to the lack of 3D Cu–O–Cu linkages as seen in Cu_2O , while in the delafossite structure there are only Cu–O–M–O–Cu linkages [110]. This statement is supported by a later report that the electrical conductivity along the ab plane of CuAlO_2 single crystal is 25 times higher than that along the c axis [111]. Similar anisotropic ratio (~ 30 times) has also been reported for CuCrO_2 single crystals [112]. Scanlon and Watson *et al* calculated the electronic structures and effective masses of CuMO_2 (M = Al, Cr, Sc and Y) using DFT corrected for on-site Coulombic interactions (GGA + U) which gives a more accurate bandgap value than GGA and LDA [113–115].

Their results show CuAlO_2 have an effective mass of $2.6 m_e$ in the ab plane, while a large effective mass of $38.95 m_e$ along the c axis. Similar anisotropy in effective masses has also been obtained for CuBO_2 [116], CuCrO_2 [114], CuScO_2 [115] and CuYO_2 [115], as summarized in table 2. It is also of interest to discuss the effect of M^{3+} cation on the trend of effective masses. As the sizes of the M^{3+} cations increase, the Cu–Cu distance (equal to the ab lattice constant) increase. The larger Cu–Cu distance reduces the dispersion at VBM and hence results in a higher effective mass. Overall all the CuMO_2 have much larger effective masses than that of Cu_2O ($0.58 m_e$ determined by experiment [84] and $0.24 m_e$ by LDA calculation [83]), which might explain much lower mobilities commonly observed in CuMO_2 .

The higher conductivity in delafossites compared to Cu_2O should be associated with the a higher hole concentrations produced by a higher density of native acceptor-like defects (e.g. V_{Cu}) and/or intentional divalent doping at M^{3+} sites. Divalent doping (e.g. Mg^{2+}) is a straightforward way to introduce hole carriers. Provided the oxygen stoichiometry is unchanged, each divalent cation substituting at M^{3+} site should in principle introduce one hole state. $\text{CuAl}_{1-x}\text{Mg}_x\text{O}_2$ [27], $\text{CuCr}_{1-x}\text{Mg}_x\text{O}_2$ [28], $\text{CuSc}_{1-x}\text{Ca}_x\text{O}_2$ [28], $\text{CuIn}_{1-x}\text{Ca}_x\text{O}_2$ [30] and $\text{CuY}_{1-x}\text{Ca}_x\text{O}_2$ [32] with $0 < x < 0.05$ have been reported showing higher conductivities than their undoped forms. An attempt has been made for doping CuGaO_2 with Mg, but was not successful [33]. To date $\text{CuCr}_{0.95}\text{Mg}_{0.05}\text{O}_2$ polycrystalline films reported by Nagarajan *et al* in 2001 have the record highest conductivity (220 S cm^{-1}) of any p -type TCOs, but the films only have 30–40% transmittance [28]. The electronic structure of CuCrO_2 has been found to be very similar to that of other Cu^+ -based oxides: Cu $3d^{10}$ intermix strongly with O $2p^6$ to form the top of VB [29, 114, 117]. The role of Cr $3d$ states has been a matter of debate, because it is experimentally difficult to pinpoint the energy position of the Cr $3d$ state [29, 105, 118]. A recent study based on resonant PES, x-ray absorption (XAS) and DFT calculations by Yokobori and co-workers suggest that the Cr $3d$ states straddle most of the top of VB and hybridize strongly with Cu $3d$ and O $2p$ states [119]. The significant Cr

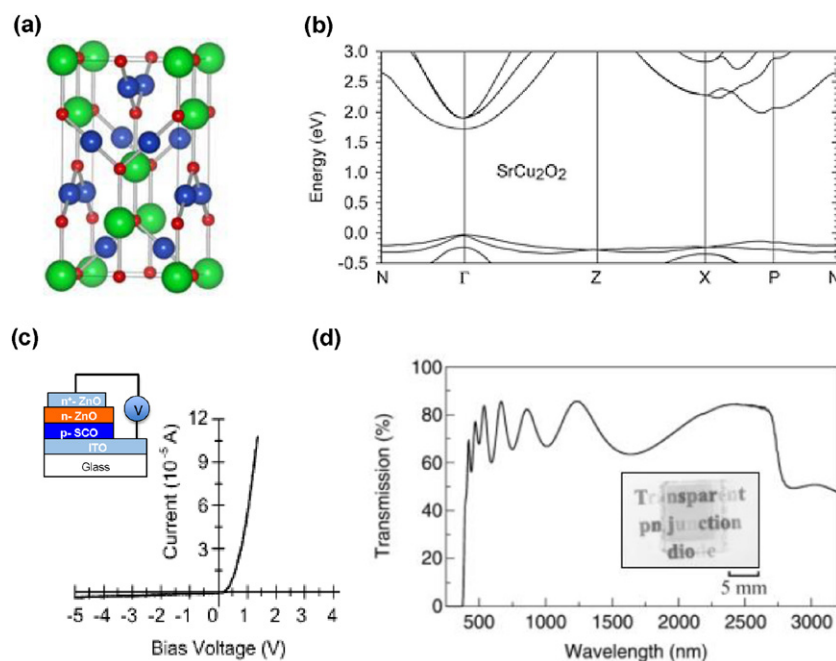


Figure 8. (a) The crystal structures of SrCu_2O_2 ; the Sr atoms are represented by large blue spheres, Cu ions by medium spheres and O ions by small spheres. (b) The bandstructure of SrCu_2O_2 along the high symmetry directions, plotted with reference to the top of the VB (0 eV). Both the VBM and CBM occur at the Γ point making it a direct gap material. (Reproduced from [129] with permission of The Royal Society of Chemistry.) (c) The structure and rectifying I - V characteristics of a transparent p - n heterojunction diode: glass/ITO/ p - SrCu_2O_2 / n - ZnO/n^+ - ZnO . ITO and degenerately doped n^+ - ZnO are used as ohmic contacts. (d) The optical transmission spectrum and photograph (inset) of the heterojunctions. (Reprinted from [131] with the permission of AIP Publishing.)

$3d$ contribution at the top of VB suggests that the holes introduced into CuCrO_2 by p -type doping are partially delocalized onto Cr [118, 119]. This possibly accounts for the higher conductivity of CuCrO_2 as compared with CuAlO_2 . Meanwhile Cr^{3+} cations at oxygen octahedrons also show d - d excitations with an energy of 2.6 eV which may explain the low transparency of CuCrO_2 [28, 104].

CuInO_2 is another material of particular interest, because it is amenable to bipolar doping, where p - or n -type doping can be achieved by Ca or Sn substitution, respectively [30, 120]. The bipolar dopability of CuInO_2 can be understood within the framework of equilibrium doping theory. According to the ‘doping limit rule’ reported by Zhang *et al*, a compound with higher VBM is easier to dope p type, while a compound with lower CBM is easier to dope n type [120]. LDA calculations indicate that the VBM of CuInO_2 is mainly composed of Cu $3d^{10}$ with some mixture of O $2p$ state, therefore explaining the p -type dopability. The CBM is mainly formed by low lying In $5s$ state in a similar way as the case for In_2O_3 , which explain the n -type dopability by Sn. The higher VBM and lower CBM results in a small fundamental bandgap for CuInO_2 , whereas the material is still optically transparent as the transitions are dipole forbidden [120]. Nevertheless there has been little to bipolar doping of CuInO_2 following [30, 121] it would be interesting to re-investigate this system based on high-quality thin films.

For nominally ‘undoped’ CuMO_2 , V_{Cu} , oxygen interstitials (O_i) and antisite (Cu_M) are believed to be the possible source of hole carriers. Perllicer-Porres *et al* [122] and Tate *et al* [111]

postulated that V_{Cu} is the dominant native defect responsible for the p -type conductivity in CuAlO_2 based on optical absorption spectra of high-quality CuAlO_2 single crystals. This is supported by DFT calculations by Katayama-Yoshida *et al* [123, 124] and Nolan [89] who report V_{Cu} has the smallest formation energy. However, recently Scanlon and Watson using more advanced hybrid-DFT have shown that besides V_{Cu} , Cu_{Al} antisites are also dominant defects under Cu-poor/Al-poor conditions [113]. Their calculations also found the transition levels of these defects are deep in the bandgap being at 0.68 eV above VBM, in agreement with the experimental value (0.70 eV) deduced from optical absorption [111]. Interestingly, as the size of M^{3+} cation increase (e.g. CuYO_2 and CuScO_2), O_i becomes more energetically favourable because of the more open lattice structure to accommodate excess oxygens [31, 125]. One O_i can trap two electrons leaving behind two hole states at the VB ($\text{O}_2(\text{g}) = 2\text{O}_i'' + 4\text{h}^\bullet$). It has been shown that CuScO_{2+x} and CuYO_{2+x} can intercalate excess oxygen up to $x > 0.5$ by annealing the materials in oxygen-rich conditions, while there is negligible excess oxygen detected in CuAlO_{2+x} ($x < 0.00002$) [98, 125]. Duan *et al* prepared CuScO_2 polycrystalline thin films on silica by sputtering and found the as-prepared films were insulating [31]. Treating the films under oxygen at 450 °C significantly increased the conductivity up to 30 S cm^{-1} , the highest conductivity reported for nominally ‘undoped’ CuMO_2 . They suggest O_i was the dominant defect for the p -type carrier in CuScO_{2+x} .

3.2.3. SrCu_2O_2 . SrCu_2O_2 does not possess a delafossite structure but can be viewed as an extension of Cu-based delafossite.

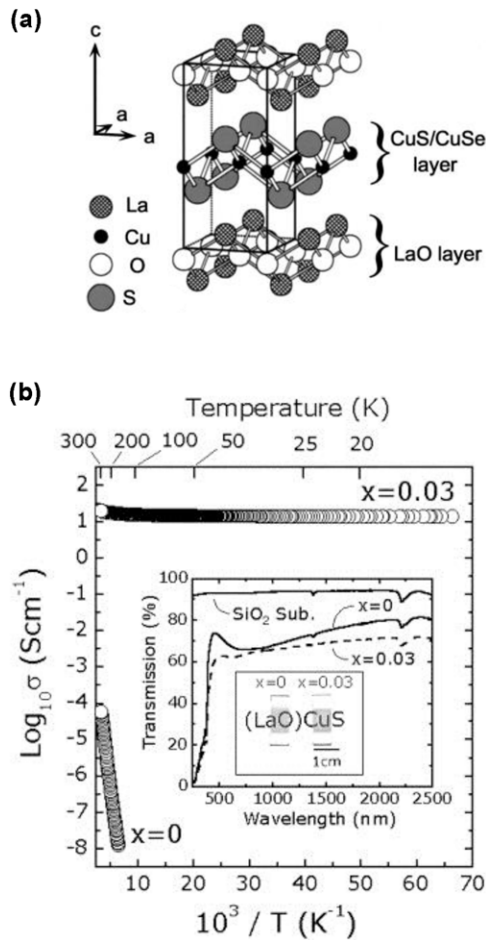


Figure 9. (a) Crystal structure of LaCuOS; where the LaO layer can be replaced by SrO leading to hole doping. (b) Temperature dependence of electrical conductivity for $\text{La}_{1-x}\text{Sr}_x\text{CuOS}$ films ($x = 0$ and 0.03). The inset shows optical transmission spectra of the films in the visible-near IR region, and photographs. (Reprinted from [137], with the permission of AIP Publishing, and from [143], copyright 2002, with permission from Elsevier.)

As shown in figure 8(a), SrCu_2O_2 crystallises in a tetragonal structure with a unit cell of $a = 5.480 \text{ \AA}$ and $c = 9.825 \text{ \AA}$. This crystal has the same O–Cu–O dumbbell zigzag chains separated by SrO_6 octahedron. It is therefore expected that reduction of dimension also leads to a large bandgap relative to Cu_2O , similar to that of Cu delafossite. Kuo *et al* prepared both undoped and 3% K doped SrCu_2O_2 thin films by PLD [34]. The undoped film showed a low p -type conductivity of $3.9 \times 10^{-3} \text{ S cm}^{-1}$ and mobility of $0.46 \text{ cm}^2 \text{ V}^{-1} \text{ s}^{-1}$. The conductivity could be slightly increased to $4.8 \times 10^{-2} \text{ S cm}^{-1}$ by 3% K doping, but the carrier concentration is still three orders of magnitude less than K doping concentration.

The electronic structure of SrCu_2O_2 have been examined by photoelectron, optical spectroscopy and DFT calculations [83, 126, 127]. The VBM is formed by the antibonding state of Cu $3d$ with O $2p$, while the CBM is primarily composed of Cu $4s$ (figure 8(b)) [128]. Godinho *et al* have performed GGA and GGA + U calculations on the electronic structure and defects of SrCu_2O_2 [129, 130]. They found the lowest hole effective masses ($0.78 m_e$) is along the $[100]$ and $[010]$ directions, i.e. the zigzag O–Cu–O dumbbell chain direction. Their results

also suggest V_{Cu} and Sr vacancies (V_{Sr}) are the most likely native defects leading to p -type conductivity in undoped films.

Optical measurements indicated that SrCu_2O_2 is a direct bandgap material ($E_g = 3.3 \text{ eV}$) [126]. This is in contrast to the case for delafossites where an indirect bandgap normally appears in the visible light region. A direct bandgap semiconductor is highly desirable for many optoelectronic devices such as light-emitting diode (LED) and laser diodes. In addition, SrCu_2O_2 thin films can be deposited at temperatures as low as 350°C , making it possible to minimize the chemical reaction. Thereafter SrCu_2O_2 have received much attention used as an active p -type semiconductor in combination with available n -type oxides to form p – n heterojunctions. Kudo *et al* have fabricated all oxide-based transparent p – n heterojunctions composed of n^+ -ZnO/ n -ZnO/ p -SCO/ITO deposited on glass substrates where the n^+ -ZnO and ITO are used as transparent electrodes, as shown in figures 8(c) and (d) [131]. The diode had an average transmission of $\geq 70\%$ in the visible spectrum (figure 7(d)). A typical current voltage (I – V) characteristic of the p – n heterojunction diode. Ohta *et al* have successfully fabricated an ultraviolet LED by epitaxially growing p - SrCu_2O_2 on n -ZnO by PLD [132]. Their p – n heterojunctions emit a sharp emission band centred at 382 nm at room temperature, which demonstrate SrCu_2O_2 can be used as an optically active p -TCO material for optoelectronic devices.

4. Layered oxychalcogenides

These Cu^+ -based ternary p -type transparent oxides still suffered from low hole concentration and low carrier mobility. As a consequence, the CMVB was also extended by using chalcogen (Ch = S, Se, and Te) elements p orbitals to replace the oxygen ones, since a more dispersed VBM was theoretically expected from stronger hybridization between Cu $3d$ and Ch p orbitals, due to the increasing covalency between Cu and Ch atoms in the sequence of O, S, Se, and Te. Following this concept, the first material being identified as a p -TCO was LaCuOS layered oxysulfide by Hosono and co-workers in 2000 [36], although the crystal structure and p -type conductivity of this material were reported by many other researchers [133]. The crystal structure of LaCuOS is composed of CuS and LaO layers alternately stacked along the c axis (figure 9(a)) [133, 134]. In the CuS layers, Cu is tetrahedrally coordinated by four S ions, forming the upper part of the VB and conduction paths for holes; the LaO layers confine the CuS in 2D layers, leading to a large bandgap of 3.1 eV [135]. Therefore LaCuOS is transparent in the visible region. The conductivity can be controlled over a wide range by substitution of La^{3+} by divalent Sr^{2+} or Mg^{2+} , in a similar way to the well-known hole-doped perovskite transition metal oxides [136]. It has been demonstrated by Hiramatsu *et al* that the hole concentrations and conductivities can be increased from $2 \times 10^{15} \text{ cm}^{-3}$ and $0.00006 \text{ S cm}^{-1}$, up to $2.7 \times 10^{20} \text{ cm}^{-3}$ and 20 S cm^{-1} respectively, by doping LaCuOS with 3% Sr at La sites (figure 9(b)) [137, 138]. The hole concentration obtained in this result is extremely high among the p -type TCOs reported. Interestingly temperature dependence of conductivity

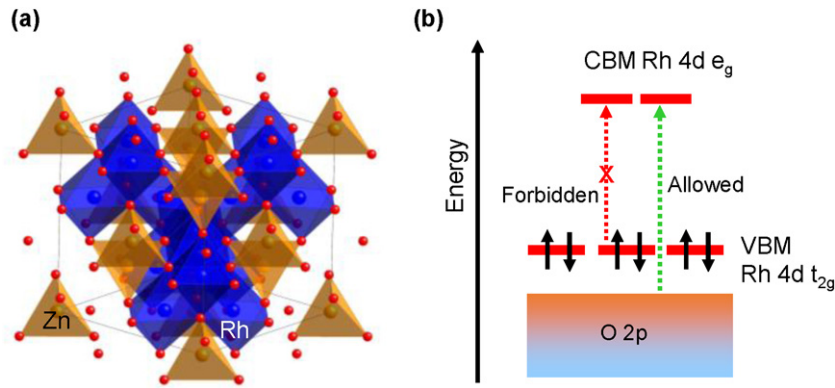


Figure 10. (a) Crystal structure of ZnRh₂O₆, where the Rh cations are coordinated by oxygen octahedrons (blue) and Zn in tetrahedrons (golden). (b) Schematic energy diagram for the Rh 3d⁶ in oxygen octahedrons.

measurement (figure 9(b)) indicate the 3% Sr doped film exhibit a degenerately doped semiconductor conduction mechanism, and thus offer promising potential for development of a high performance *p*-TCO to rival their *n*-type counterparts.

In addition to these wide-gap and conducting properties, a PL spectra study also indicated LaCuOS has a direct allowed bandgap [37, 135]. Due to its large exciton binding energy (~59 meV), LaCuOS emits UV light associated with excitons at room temperature, which makes LaCuOS a unique material similar to ZnO but of *p*-type character. This notable property offers promise as an active layer in optoelectronic applications such as UV or violet LEDs [12, 139].

Furthermore, the bandgap of LnOCuCh can be largely tuned by controlling the chemical compositions at Ch sites [140]. The bandgaps decrease from 3.1 eV for LaOCuS, 2.82 eV for LaOCuSe and 2.31 eV for LaOCuTe [141, 142]. The chemical trend of the bandgaps can be simply understood from the decrease of the energy levels of Ch *np*⁶ orbitals (S > Se > Te): Ch *np*⁶ form the top of the VB with Cu 3d¹⁰ orbital. Hosono and co-workers have prepared LaCuOS_{1-x}Se_x (*x* = 0, 0.25, 0.50, 0.75, 1.0) solid solutions in the form of polycrystalline bulk and epitaxial thin films, and found their bandgaps change almost linearly from 3.1 eV to 2.8 eV as *x* varies from 0 to 1 [38, 143]. The Hall mobility increases as the concentration of Se and reaches 8.0 cm² V⁻¹ s⁻¹ in LaCuOSe. A remarkably high hole density of 1.7 × 10²¹ cm⁻³ and a room temperature conductivity of 910 S cm⁻¹ has been achieved on Mg-doped LaCuOSe epitaxial films [144]. Unfortunately this material shows low transmittance for visible light because of the smaller bandgap of LaCuOSe (2.8 eV) and absorption arising from in-gap hole states, making it not suitable as a *p*-TCO.

Recently, Liu *et al* have synthesized Sr₃Cu₂Sc₂O₅S₂ polycrystalline bulks as a *p*-type TCOs [40]. Its structure also belongs to layered oxysulfide, composed of similar 2D CuS slabs confined by perovskite-like Sr₃Sc₂O₅. The authors showed this material has a wide energy gap of 3.1 eV (but also with strong absorption at lower energy), an intrinsic *p*-type conductivity of 2.8 S cm⁻¹ and a remarkable high mobility of 150 cm² V⁻¹ s⁻¹, even higher than the highest mobility reported for *n*-type TCO. Scanlon *et al* have performed GGA + *U* and HSE06 calculations on the electronic structure of Sr₃Cu₂Sc₂O₅S₂ [145]. Their results suggests this material

has a direct optical band gap of ~3.5 eV. Detailed analysis of the bandstructure indicated a strong mixing of the S 3*p* states and the Cu 3*d* states at the VBM is the cause of the high mobility in agreement with the experimental result by Liu *et al*. It is undoubtedly of significant interest to prepare this material into thin films and dope it with monovalent cations (K⁺) at Sr sites or divalent (Mg²⁺) at Sc sites to improve the conductivity in this material.

5. Spinel oxides (*nd*⁶)

The essence of chemical design concept is to modulate the top of the VB by intermixing oxygen 2*p*⁶ with closed shell Cu 3*d*¹⁰ orbitals to reduce localization of holes in oxygen ions and meanwhile avoid colorization from metal *d*-*d* excitation. This concept also leads to the idea that transition metal ions (Co³⁺, Rh³⁺ and Ir³⁺) with a *d*⁶ configuration in an octahedral oxygen coordination may behave similarly to Cu 3*d*¹⁰, since their low spin ground states could be regarded as a 'quasi-closed' shell configuration. As shown in figure 10(b), the *d* orbital is the octahedral ligand field splits *d* orbital into sixfold degenerate *t*_{2g} and fourfold degenerate *e*_g states. The *t*_{2g} states are fully occupied by all six electrons with low spin configuration forming the top of VB, while the empty *e*_g states form CBM. Following this concept, a new class of non-*d*¹⁰ *p*-TCO, ZnM₂O₄ (M = Co, Rh, and Ir) were identified [41, 146]. ZnM₂O₄ have a normal spinel crystal structure (figure 10(a)) with Zn occupying the tetrahedral sites and M occupying the octahedral sites. Mizoguchi *et al* first reported ZnRh₂O₄ thin film exhibited *p*-type TCO behaviour with an electrical conductivity of 0.7 S cm⁻¹ with no intentional doping and a bandgap of 2.1 eV [147]. The authors also confirmed that the electronic configuration of Rh 4*d*⁶ was in the low spin state of *t*_{2g}⁶ · *e*_g⁰ by magnetic susceptibility measurement and the bandgap is indeed defined by the fully filled *t*_{2g}⁶ state hybridizing with some O 2*p* (VB) and empty *e*_g⁰ orbital (CB) using photoemission spectroscopy. Despite the small bangap of 2.1 eV, ZnRh₂O₄ shows transparency to visible light because the bandgap is of *d*-*d* character whose transition is dipole forbidden. Unlike Cu-delafoossites where the O-Cu-O dumbbells are confined in two-dimensions, the RhO₆ octahedra in

ZnRh₂O₆ are tightly connected through edge-sharing into a 3D structure. This enhances the hybridization between metal *d* and O 2*p* orbitals, and thus the hole conduction path is 3D. As a consequence, it has been demonstrated that the amorphous ZnRh₂O₄ thin films retain its *p*-type character when used in a *p*-*n* diode based on amorphous ZnRh₂O₄ on amorphous *n*-type InGaZnO₄ [146]. The *p*-type conduction in the amorphous structure might originate from the isotropic nature of the spinel structure and the edge-sharing RhO₆ networks, which are less affected by the structural disorder and are even stable in an amorphous network.

After the pioneering of ZnRh₂O₄, Dekkers *et al* reported the growth of *p*-type ZnCo₂O₄, ZnRh₂O₄ and ZnIr₂O₄ polycrystalline and epitaxial thin films by PLD [41]. Conductivities of 0.39 S cm⁻¹ (0.61 S cm⁻¹), 2.75 S cm⁻¹ (2.83 S cm⁻¹) and 3.39 S cm⁻¹ (2.09 S cm⁻¹) are obtained for polycrystalline (epitaxial) films of ZnCo₂O₄, ZnRh₂O₄, and ZnIr₂O₄, respectively. Based on optical absorption spectra, the authors also showed the bandgaps of ZnCo₂O₄, ZnRh₂O₄, and ZnIr₂O₄ are 2.26 eV, 2.74 eV, and 2.97 eV. The increase of bandgaps (Co < Rh < Ir) is argued due to the increasing crystal field splitting between *t*_{2g} and *e*_g in going from 3*d*(Co) < 4*d*(Rh) < 5*d*(Ir). However, the magnitude and trend of bandgaps reported by Dekkers are at variance with other experiments and theoretical works. For example, the bandgap of ZnRh₂O₄ has been measured to be 2.1 eV by Mansourian-Hadavi *et al* [148] and 1.2 eV by Sing *et al* [149], while the values from DFT dependent on calculation methods range from 0.8 eV to 3.2 eV [150, 151]. A re-investigation of the optical and electronic structure of these materials based on high-quality thin films is thus needed to resolve these fundamental issues.

ZnCo₂O₄ is probably the most studied of ZnM₂O₄ spinels, with much interest generated due to its possible applications in photo-(electro-)catalysis [152–154], supercapacitors [155] and Li ion batteries [156, 157]. Kim *et al* reported ZnCo₂O₄ has an optical band gap of 2.63 eV, and can show both *p*-type (a conductivity of up to 21 S cm⁻¹) and *n*-type conductivity by controlling the oxygen pressure [158]. Recently, Grundmann and co-workers demonstrated amorphous *p*-*n* junction diodes and field-effect transistors using *p*-type ZnCo₂O₄ deposited at room temperature, indicating potential of this material for oxide electronic applications [159–161].

There is general consensus that the intrinsic *p*-type conductivity of ZnM₂O₄ originates from the acceptor-like antisite defects Zn_M and/or Zn vacancy (*V*_{Zn}) [150, 151]. DFT calculations also found no significant dispersion in VBM and a large hole effective masses. Perkins *et al* found a hole effective mass of 18 *m*_e for ZnCo₂O₄ and this a small mobility of 0.028 cm² V⁻¹ s⁻¹ by combining DFT calculations and experimental measurements on polycrystalline sample [162]. The polaronic conduction mechanism generally found on ZnM₂O₄ may be the limiting factor for high electrical conductivity. The high price of precious Rh and Ir metal also constraint their large-scale production for industrial applications.

6. Cr-based oxides (3*d*³)

Continuing with the idea of quasi-closed shell, Cr³⁺ with a *d*³ in an octahedral oxygen coordination should give a similar electronic configuration at the VBM as *d*⁶ and *d*¹⁰ materials. The oxygen octahedral field splits Cr 3*d* orbitals into an occupied *t*_{2g}³ level forming the top of the VB, and an empty *t*_{2g}⁰ and two empty *e*_g⁰ levels forming the bottom of the CB. Cr₂O₃ and LaCrO₃ are two Cr-based oxide identified as potential *p*-type TCO [163, 164]. Cr₂O₃, also known as chromia (mineral name Eskolaite), crystallizes in the corundum structure with hexagonal closed packed layers of oxygen atoms and two-thirds of the octahedral sites filled with Cr atoms. The optical bandgap of Cr₂O₃ is reported to be 3.4 eV, arising from the strong excitation from O 2*p* to Cr *t*_{2g} and *e*_g [165, 166]. Below this strong absorption, Cr₂O₃ also shows two weak absorptions at 2.0 eV and 2.6 eV, which are usually attributed to dipole-forbidden *d*–*d* transition from occupied *t*_{2g} to empty *e*_g levels and is responsible for the green color of Cr₂O₃ powders but are weak enough not to reduce the transparency of the material in thin film form. Stoichiometric Cr₂O₃ is usually highly insulating, although there are reports of very low native *p*-type conductivity arising from Cr vacancies. Uekawa and Kaneko have reported doping Cr₂O₃ polycrystalline with Li⁺, Mg²⁺, Ni²⁺ etc at Cr site can enhance the *p*-type conductivity by introducing hole state at the top of VB, i.e. at the Cr 3*d t*_{2g} [167]. Arca *et al* was the first who demonstrated the use of Cr₂O₃ thin films as a *p*-type TCOs [163]. They found Mg and N co-doped Cr₂O₃ produced a *p*-type oxide with conductivity of 0.33 S cm⁻¹ and transmission up to 65% for a 150 nm thick film. A detailed analysis on epitaxial Mg:Cr₂O₃ films grown on Al₂O₃ by the same group showed a small polaron hopping conduction being the limiting factor in the material's conductivity [168, 169].

Recently Zhang *et al* have reported perovskite Sr-doped LaCrO₃ (La_{1-x}Sr_xCrO₃) with high FoM as new *p*-type TCOs [164]. The authors have shown that the lowest excitation in LaCrO₃ results from a *t*_{2g}³ → *e*_g⁰ transition is at ≈2.8 eV but formally dipole-forbidden. The strongest optical absorption resulting from O 2*p* to Cr *e*_g⁰ falls at ≈4.6 eV, which makes undoped LaCrO₃ highly transparent but insulating [170]. Substituting Sr²⁺ for La³⁺ in LCO effectively dopes holes into the top of the VB and results in *p*-type conductivity (figures 11(b) and (c)) [171]. The perovskite structure represents an advantage for this material, because it allows one more easily to dope it and integrate with the workhorse of other perovskite oxides which exhibit interesting properties such as high superconducting temperature superconductors, colossal magnetoresistance and ferroelectricity [136]. It has been shown the *p*-type LaCrO₃ films can form isostructural and coherent interface with the well-known *n*-type SrTiO₃, see figure 11(a). XPS reveals that the LaCrO₃/SrTiO₃ heterojunction exhibits a type-II staggered band alignment [172]. In contrast, the transparent *p*-*n* junctions fabricated using *p*-type CuMO₂ delafossites and *n*-type ZnO form much more defective interfaces because of their very different crystal symmetries. These considerations

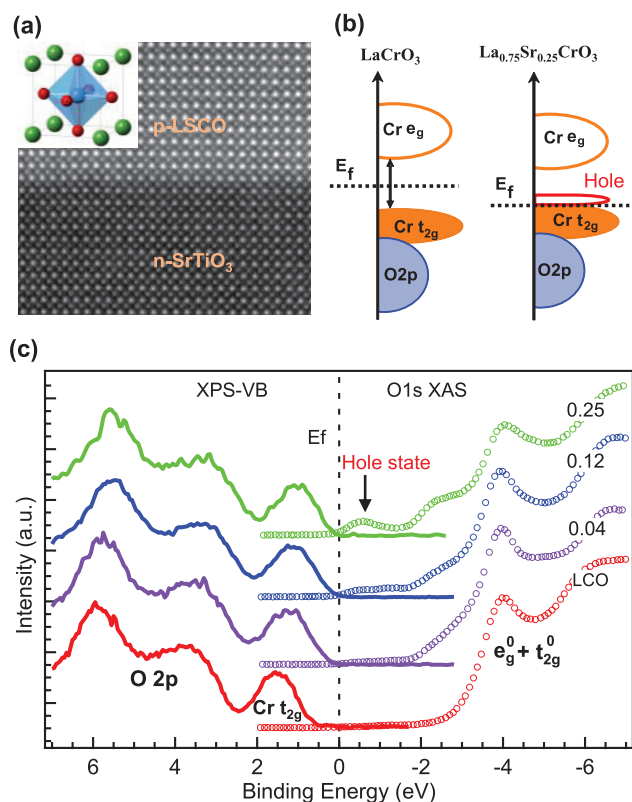


Figure 11. (a) A cross-sectional HRTEM image of the $\text{La}_{0.75}\text{Sr}_{0.25}\text{CrO}_3$ grown on SrTiO_3 (001) substrate. Inset shows the crystal structure of a perovskite. (b) Schematic energy diagram for LaCrO_3 and $\text{La}_{0.75}\text{Sr}_{0.25}\text{CrO}_3$. (c) Combination of XPS VB (left) and O K-edge XAS spectra (right) to map out the evolution of electronic structure of $\text{La}_{1-x}\text{Sr}_x\text{CrO}_3$ as function of Sr doping. The intensity of hole state at the top of VB increase with increasing of Sr doping. (Reprinted with permission from [164].)

have implications for the fabrication of all-perovskite oxide transparent electronic devices.

7. Lone pair based oxides (ns^2)

The chemistry of post-transition metals is dominated by the group oxidation state N and a lower $N-2$ oxidation state. The $N-2$ state is associated with occupation of a metal cation ns^2 lone pair (e.g. Sn^{2+} and Bi^{3+}). The ns^2 lone pair can interact strongly with O $2p$ by distorting the lattice, forming antibonding states at the top of VB [173–175]. Because cation s orbitals are generally more spatially extended than d states, it is therefore expected that their hybridization with O $2p$ states can result in lower effective mass (in a way similar to the case of n -type TCOs). SnO (Sn^{2+} : $5s^2$) is one of the material that has been receiving considerable attentions as a p -type semiconductor [11, 42, 176–179]. The stable phase of SnO adopts a layered tetragonal structure (litharge), space group $P4/nmm$, with each Sn atom positioned at the apex of a square pyramid formed by four oxygen atoms (figure 12(a)). The Sn and O atoms arranged alternatively with layered structure in a $\text{Sn}_{1/2}\text{--O--Sn}_{1/2}$ layer sequence. The lone-pair Sn $5s^2$ is projected out into the void space between the $\text{Sn}_{1/2}$ layers along the $[001]$ crystallographic direction. The formation of

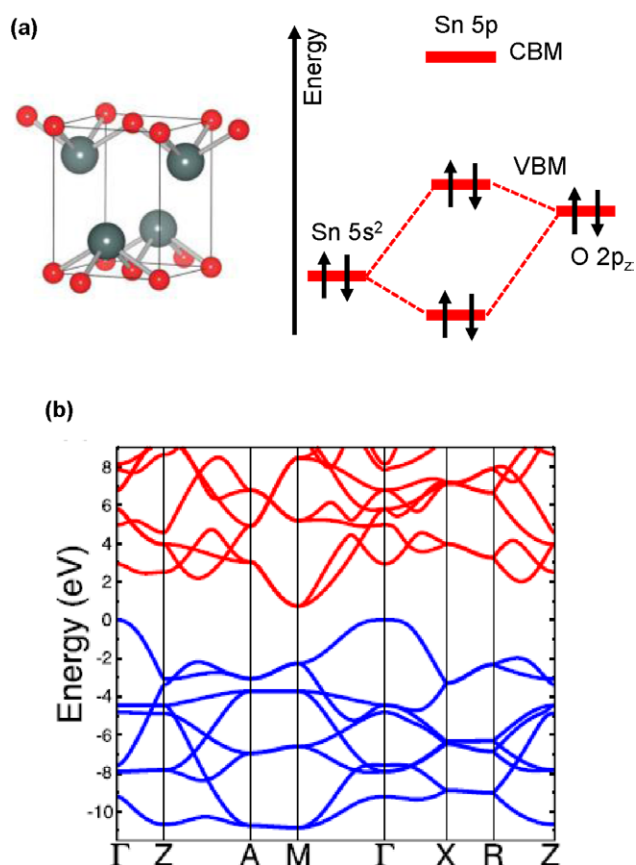


Figure 12. (a) Crystal structure and energy diagram of SnO ; (b) Bandstructure of SnO along high-symmetry directions calculated with the HSE hybrid functional, showing indirect bandgap. (Reprinted from [181] with the permission of AIP Publishing.)

a distortion in the lattice allows significant mixing between Sn $5s$ and O $2p$ states, giving rise to a filled antibonding state with some $5s$ character at the top of the VB [180, 181]. This situation is clearly manifested in the bandstructure of SnO calculated by DFT, showing a dispersive VBM at Γ -point, and interestingly dispersive CBM at M point (figure 12) [39, 180, 181]. The dispersive CBM can be understood the low lying Sn $5p$ state hybridized with Sn $5s$. Therefore the DFT calculations reveal that SnO has an ‘indirect’ fundamental bandgap of 0.61 eV between the Γ - and M-points. The direct bandgap with strong optical absorption is reported to be between 2.6–3.2 eV, which explains the reasonable transparency of SnO .

The interest in SnO was sparked by Ogo and co-workers who grew SnO epitaxial films on yttria-stabilized zirconia (YSZ) substrates by PLD in 2008, showing a Hall mobility of $2.4 \text{ cm}^2 \text{ V}^{-1} \text{ s}^{-1}$ and a field-effect mobility of $1.3 \text{ cm}^2 \text{ V}^{-1} \text{ s}^{-1}$ when used as a p -channel TFT. Subsequently both epitaxial and polycrystalline thin films have been fabricated several groups using a variety of technique such as PLD, sputtering and e-beam evaporation [11, 42, 176–179]. All the results show SnO thin films have intrinsic p -type conductivity with a Hall mobility around $1\text{--}5 \text{ cm}^2 \text{ V}^{-1} \text{ s}^{-1}$. Furthermore, Hosono *et al* have shown n -type SnO can be achieved by Sb doping with a mobility of $2 \text{ cm}^2 \text{ V}^{-1} \text{ s}^{-1}$, which makes SnO as a promising bipolar conductor for n - and p -type TFTs and

p - n junctions [177, 182]. However the issue with SnO is that SnO is very unstable and can be easily either over-oxidized into SnO₂ or reduced into metallic Sn. It is still challenging to deposit a single-phase thin film. Controlling its surface/interface represents another challenge for device fabrication.

Ba₂BiTaO₆ is another interesting novel p -TCOs taking advantage of the Bi 6s² lone pair state, which has been recently identified through a high-throughput computational screening methodology by Hautier and co-workers [26, 43]. Ba₂BiTaO₆ has a rhombohedral double perovskite structure, containing an ordered array of Bi³⁺ and Ta⁵⁺ ('B-site') octahedral surrounded by Ba²⁺ ('A-site'). Their calculations show that the Bi³⁺ with filled 6s² orbitals hybridizes strongly with O 2p, increasing the extent of the dispersion at VBM and effectively reducing the valence effective mass, while Ta⁵⁺ forms a CBM with low electronegativity, leading to a large bandgap (>3.8 eV) for optical transparency. The authors also synthesized Ba₂BiTaO₆ thin films by PLD [43]. The results confirmed high transparency (>90%) in the visible region and a high hole mobility of >30 cm² V⁻¹ s⁻¹, but carrier concentration is low at only 5×10^{13} cm⁻³. Nevertheless the Ba₂BiTaO₆ has the ubiquitous perovskite structure, which offers a wide range of possibility of integrations with other functional perovskite materials. This research highlights the importance of high-throughput computations to provide material scientists with new angles to attack the challenge in materials discovery [183].

8. NiO (3d⁸)

NiO is a well-known p -type semiconductor with a rock-salt type crystal structure and an optical bandgap of around 3.4–4.0 eV [184]. It was actually the first known p -TCO as reported by Sato *et al* in 1993, who prepared Ni_{1-x}O thin films by RF magnetron sputtering [185]. Their films show a conductivity up to 7.1 S cm⁻¹ and a moderate transmittance of 40% in the visible region. Stoichiometric NiO is highly insulating; the p -type conductivity is believed to be due to hole states induced by Ni vacancies (V_{Ni}) formed in oxygen-rich conditions. Doping NiO with Li⁺ at Ni sites (Li_xNi_{1-x}O) is another way to enhance conductivity and has been extensively studied for a long time [186–188]. It was found if the doping is less than 0.25, the Li⁺ ions randomly replace Ni sites without changing the crystal structure. Each Li⁺ ion in principle donates one hole state to the top of the VB, although whether the hole state is of Ni³⁺ or O character is a matter of much debate because of the strong electron correlation in this system [186, 189, 190]. Electron correlations resulting from the nature of Ni 3d orbitals is a main factor limiting the conductivity of Ni_{1-x}O or Li_xNi_{1-x}O. The highest conductivities reported for Ni_{1-x}O and Li_xNi_{1-x}O are 7.1 S cm⁻¹ [188, 191]. All the temperature-dependent conductivity data show thermally-activated Arrhenius behaviour. It is still debated whether the conduction is through a band-like or small polaron mechanism [192]. Chen *et al* reported that a high p -type Hall mobility of 28.56 cm² V⁻¹ s⁻¹ could be achieved by RF sputtering [193]. However, one should keep in mind that to

get a reliable Hall mobility on p -type oxides is a nontrivial problem, because of the very lower mobility values ($\ll 1$ cm² V⁻¹ s⁻¹). Regardless of its low conductivity, NiO is likely the most widely used p -type TCOs. Similar to others p -TCOs discussed above, NiO has been used in electronic devices, such as TFTs and p - n diodes [194–197]. The simple rocksalt structure is one of the advantage for NiO, as this makes it more compatible to be integrated with other n -type materials. Ohta *et al* have fabricated all single-crystalline transparent p - n heterojunction diode composed of p -NiO and n -ZnO epitaxially grown on YSZ(1 1 1) substrates by PLD. The diode exhibited clear rectifying I - V characteristics with a forward threshold voltage of 1 V. An efficient UV response was observed up to 0.3 A W⁻¹ at 360 nm, comparable to those of commercial GaN UV detectors [195]. Apart from these, NiO also shows promising applications in electrochromics for smart windows [198, 199], resistive switching memory [200, 201], and hole transport layer for solar cells [202, 203].

9. Summary and remarks

In this article, we provided a review on the fundamental materials physics of traditional and recently emergent p -type TCOs, including Cu 3d¹⁰, Ni 3d⁸, Nd⁶, Cr 3d³ and post-transition metal ns^2 based oxide materials. In essence, the key strategy for achieving a superior p -type TCO is to delocalize the top of VB by enhancing the orbital hybridization between O 2p and metal cations. This field has witnessed a steady development since the seminal report by Hosono and co-workers in 1997. Remarkable advances in transparent oxide semiconductor for (opto-)electronic devices have been achieved by using p -type TCOs or along with traditional n -type ones for transistors, UV LED and lasers, detectors and photovoltaics. However, the overall performance of p -TCOs is still far behind their n -type counterparts, as illustrated in figure 4. Using anions (such as S²⁻, Se²⁻, P³⁻) with p -orbitals more delocalized than oxygen and post transition metal ns^2 lone pair states (Sn²⁺, Pb²⁺ and Bi³⁺) would be a promising way for design of new p -type materials with superior performance. Meanwhile, the use of high-throughput computations also provides scientists with new angles to design materials in a more rational way. This is manifested by the initial study by Hautier *et al* who screened over 3000 compounds and identified Ba₂BiTaO₆ [26, 43]. Another recent computational screening by Yan *et al* lead to the identification of TaIrGe (half-Heusler) as a new p -type TCO with a bandgap of 3.36 eV and remarkably high hole mobility of 2730 cm² V⁻¹ s⁻¹ [204].

Additionally we also discussed the chemistry of defects/doping in these materials based on recent computational simulations and experimental data. There is satisfactory understanding in the literature on the microscopic mechanism of the energetics of defects, the transition energy levels, and the corresponding macroscopic transport properties. A domain which remains largely unexplored, but of particular interest, is the surface and interface chemistry of the p -type TCOs, especially Cu₂O and SnO [42, 63]. Many research works have

implied that the trap states formed at the interface are the key factor limiting the use of these materials for TFT and photo-voltaic cells [77, 78, 80].

Lastly we would like to point out that the selection criteria for p -type TCOs should be tightly related to the purpose of its applications. For (opto-)electronic devices such as transparent TFT and p - n diodes, a high mobility but low hole concentration is preferred. For use as hole transport layer in photo-voltaic cells, a high hole conductivity and transparency for violet to near-infrared wavelengths become more important. This criteria does not require the materials directly have high mobility and visible light transparency. Hole-doped transition metal oxides emerge to meet this requirement, as these type of materials can be amendable to achieve a high hole carriers concentration at the d orbitals. For example $n = 7.5 \times 10^{21} \text{ cm}^{-3}$ and $2.2 \times 10^{22} \text{ cm}^{-3}$ have been achieved in Sr doped LaCrO_3 [164] and SrVO_3 [205], respectively, while transparency is still maintained by the dipole forbidden transitions.

Acknowledgments

KHL Zhang acknowledges the funding support from Herchel Smith Postdoctoral Fellowship by University of Cambridge.

References

- [1] Yu X G, Marks T J and Facchetti A 2016 *Nat. Mater.* **15** 383–96
- [2] Ellmer K 2012 *Nat. Photon.* **6** 808–16
- [3] Fortunato E, Ginley D, Hosono H and Paine D C 2007 *MRS Bull.* **32** 242–7
- [4] Barquinha R M P, Pereira L and Fortunato E 2012 *Transparent Oxide Electronics: From Materials to Devices* 1st edn (Chichester: Wiley)
- [5] Minami T 2005 *Semicond. Sci. Technol.* **20** S35–44
- [6] Granqvist C G 2007 *Sol. Energy Mater. Sol. Cells* **91** 1529–98
- [7] Frank G, Kauer E and Kostlin H 1981 *Thin Solid Films* **77** 107–17
- [8] Hoffman R L, Norris B J and Wager J F 2003 *Appl. Phys. Lett.* **82** 733–5
- [9] Nomura K, Ohta H, Ueda K, Kamiya T, Hirano M and Hosono H 2003 *Science* **300** 1269–72
- [10] Nomura K, Ohta H, Takagi A, Kamiya T, Hirano M and Hosono H 2004 *Nature* **432** 488–92
- [11] Fortunato E, Barquinha P and Martins R 2012 *Adv. Mater.* **24** 2945–86
- [12] Ohta H and Hosono H 2004 *Mater. Today* **7** 42–51
- [13] Pan Z W, Dai Z R and Wang Z L 2001 *Science* **291** 1947–9
- [14] Comini E, Faglia G, Sberveglieri G, Pan Z W and Wang Z L 2002 *Appl. Phys. Lett.* **81** 1869–71
- [15] Batzill M and Diebold U 2005 *Prog. Surf. Sci.* **79** 47–154
- [16] Baedeker K 1907 *Ann. Phys., Lpz.* **327** 749
- [17] Mudd J J, Lee T L, Munoz-Sanjose V, Zuniga-Perez J, Hesp D, Kahk J M, Payne D J, Egdel R G and McConville C F 2014 *Phys. Rev. B* **89** 035203
- [18] King P D C, Veal T D, McConville C F, Zuniga-Perez J, Munoz-Sanjose V, Hopkinson M, Rienks E D L, Jensen M F and Hofmann P 2010 *Phys. Rev. Lett.* **104** 256803
- [19] McMaster M A 1947 (Libby-Owens-Ford) (filed 5 October 5 1942) *US Patent* 2429
- [20] Edwards P P, Porch A, Jones M O, Morgan D V and Perks R M 2004 *Dalton Trans.* **2995**–3002
- [21] Exarhos G J and Zhou X D 2007 *Thin Solid Films* **515** 7025–52
- [22] Loh K P, Bao Q L, Eda G and Chhowalla M 2010 *Nat. Chem.* **2** 1015–24
- [23] Kawazoe H, Yanagi H, Ueda K and Hosono H 2000 *MRS Bull.* **25** 28–36
- [24] Banerjee A N and Chattopadhyay K K 2005 *Prog. Cryst. Growth Charact. Mater.* **50** 52–105
- [25] Kawazoe H, Yasukawa M, Hyodo H, Kurita M, Yanagi H and Hosono H 1997 *Nature* **389** 939–42
- [26] Hautier G, Miglio A, Ceder G, Rignanese G M and Gonze X 2013 *Nat. Commun.* **4** 2292
- [27] Yanagi H, Inoue S, Ueda K, Kawazoe H, Hosono H and Hamada N 2000 *J. Appl. Phys.* **88** 4159–63
- [28] Nagarajan R, Draeseke A D, Sleight A W and Tate J 2001 *J. Appl. Phys.* **89** 8022–5
- [29] Arnold T *et al* 2009 *Phys. Rev. B* **79** 075102
- [30] Yanagi H, Hase T, Ibuki S, Ueda K and Hosono H 2001 *Appl. Phys. Lett.* **78** 1583–5
- [31] Duan N, Sleight A W, Jayaraj M K and Tate J 2000 *Appl. Phys. Lett.* **77** 1325–6
- [32] Jayaraj M K, Draeseke A D, Tate J and Sleight A W 2001 *Thin Solid Films* **397** 244–8
- [33] Ueda K, Hase T, Yanagi H, Kawazoe H, Hosono H, Ohta H, Orita M and Hirano M 2001 *J. Appl. Phys.* **89** 1790–3
- [34] Kudo A, Yanagi H, Hosono H and Kawazoe H 1998 *Appl. Phys. Lett.* **73** 220–2
- [35] Ohta H, Kawamura K, Orita M, Hirano M, Sarukura N and Hosono H 2000 *Appl. Phys. Lett.* **77** 475–7
- [36] Ueda K, Inoue S, Hirose S, Kawazoe H and Hosono H 2000 *Appl. Phys. Lett.* **77** 2701–3
- [37] Ueda K, Inoue S, Hosono H, Sarukura N and Hirano M 2001 *Appl. Phys. Lett.* **78** 2333–5
- [38] Hiramatsu H, Ueda K, Ohta H, Hirano M, Kamiya T and Hosono H 2003 *Appl. Phys. Lett.* **82** 1048–50
- [39] Allen J P, Scanlon D O, Piper L F J and Watson G W 2013 *J. Mater. Chem. C* **1** 8194–208
- [40] Liu M L, Wu L B, Huang Q, Chen L D and Chen I W 2007 *J. Appl. Phys.* **102** 116108
- [41] Dekkers M, Rijnders G and Blank D H A 2007 *Appl. Phys. Lett.* **90** 3
- [42] Ogo Y, Hiramatsu H, Nomura K, Yanagi H, Kamiya T, Hirano M and Hosono H 2008 *Appl. Phys. Lett.* **93** 032113
- [43] Bhatia A *et al* 2016 *Chem. Mater.* **28** 30–4
- [44] Walsh A *et al* 2008 *Phys. Rev. Lett.* **100** 167402
- [45] Zhang K H L, Lazarov V K, Veal T D, Oropeza F E, McConville C F, Egdel R G and Walsh A 2011 *J. Phys.: Condens. Matter* **23** 334211
- [46] Lyons J L, Janotti A and Van de Walle C G 2009 *Appl. Phys. Lett.* **95** 252105
- [47] Fan J C, Sreekanth K M, Xie Z, Chang S L and Rao K V 2013 *Prog. Mater. Sci.* **58** 874–985
- [48] Bierwagen O and Speck J S 2012 *Appl. Phys. Lett.* **101** 4
- [49] Zhang K H L, Egdel R G, Offi F, Iacobucci S, Petaccia L, Gorovikov S and King P D C 2013 *Phys. Rev. Lett.* **110** 056803
- [50] Haacke G 1976 *J. Appl. Phys.* **47** 4086–9
- [51] Gordon R G 2000 *MRS Bull.* **25** 52–7
- [52] Zunger A 2003 *Appl. Phys. Lett.* **83** 57–9
- [53] Zhang S B, Wei S H and Zunger A 2001 *Phys. Rev. B* **63** 075205
- [54] Zhang S B, Wei S H and Zunger A 1998 *J. Appl. Phys.* **83** 3192–6
- [55] Robertson J and Clark S J 2011 *Phys. Rev. B* **83** 075205
- [56] Meyer B K *et al* 2013 *Oxide Semiconductors* vol 88, ed B G Svensson *et al* (San Diego, CA: Elsevier Academic) pp 201–26
- [57] Zuo J M, Kim M, O’Keeffe M and Spence J C H 1999 *Nature* **401** 49–52

- [58] Buljan A, Lluell M, Ruiz E and Alemany P 2001 *Chem. Mater.* **13** 338–44
- [59] Rai B P 1988 *Solar Cells* **25** 265–72
- [60] Katayama J, Ito K, Matsuoka M and Tamaki J 2004 *J. Appl. Electrochem.* **34** 687–92
- [61] Paracchino A, Laporte V, Sivula K, Gratzel M and Thimsen E 2011 *Nat. Mater.* **10** 456–61
- [62] Meyer B K *et al* 2012 *Phys. Status Solidi b* **249** 1487–509
- [63] Matsuzaki K, Nomura K, Yanagi H, Kamiya T, Hirano M and Hosono H 2008 *Appl. Phys. Lett.* **93** 202107
- [64] Fortunato E, Figueiredo V, Barquinha P, Elamurugu E, Barros R, Goncalves G, Park S H K, Hwang C S and Martins R 2010 *Appl. Phys. Lett.* **96** 192102
- [65] Balasubramaniam K R, Kao V M, Ravichandran J, Rossen P B, Siemons W and Ager J W 2012 *Thin Solid Films* **520** 3914–7
- [66] Seiler W, Millon E, Perriere J, Benzerga R and Boulmer-Leborgne C 2009 *J. Cryst. Growth* **311** 3352–8
- [67] Li B S, Akimoto K and Shen A 2009 *J. Cryst. Growth* **311** 1102–5
- [68] Nam D W, Cho I T, Lee J H, Cho E S, Sohn J, Song S H and Kwon H I 2012 *J. Vac. Sci. Technol. B* **30** 060605
- [69] Saji K J, Populoh S, Tiwari A N and Romanyuk Y E 2013 *Phys. Status Solidi a* **210** 1386–91
- [70] Lee Y S, Winkler M T, Siah S C, Brandt R and Buonassisi T 2011 *Appl. Phys. Lett.* **98** 192115
- [71] Minami T, Nishi Y and Miyata T 2014 *Appl. Phys. Lett.* **105** 212104
- [72] Minami T, Nishi Y, Miyata T and Nomoto J 2011 *Appl. Phys. Express* **4** 3
- [73] Kim S Y, Ahn C H, Lee J H, Kwon Y H, Hwang S, Lee J Y and Cho H K 2013 *ACS Appl. Mater. Interfaces* **5** 2417–21
- [74] Nagai H, Suzuki T, Hara H, Mochizuki C, Takano I, Honda T and Sato M 2012 *Mater. Chem. Phys.* **137** 252–7
- [75] Munoz-Rojas D, Jordan M, Yeoh C, Marin A T, Kursumovic A, Dunlop L A, Iza D C, Chen A, Wang H and Driscoll J L M 2012 *AIP Adv.* **2** 7
- [76] Bergerot L, Jimenez C, Chaix-Pluchery O, Rapenne L and Deschamps J L 2015 *Phys. Status Solidi a* **212** 1735–41
- [77] Ran F Y, Hiramatsu H, Hosono H, Kamiya T and Taniguti M 2015 *J. Vac. Sci. Technol. B* **33** 051211
- [78] Lee S W, Lee Y S, Heo J, Siah S C, Chua D, Brandt R E, Kim S B, Mailoa J P, Buonassisi T and Gordon R G 2014 *Adv. Energy Mater.* **4** 1301916
- [79] Hoye R L Z, Brandt R E, Ievskaya Y, Heffernan S, Musselman K P, Buonassisi T and MacManus-Driscoll J L 2015 *APL Mater.* **3** 020901
- [80] Lee Y S, Chua D, Brandt R E, Siah S C, Li J V, Mailoa J P, Lee S W, Gordon R G and Buonassisi T 2014 *Adv. Mater.* **26** 4704–10
- [81] Hu J P, Payne D J, Egdel R G, Glans P A, Learmonth T, Smith K E, Guo J and Harrison N M 2008 *Phys. Rev. B* **77** 155115
- [82] Ruiz E, Alvarez S, Alemany P and Evarestov R A 1997 *Phys. Rev. B* **56** 7189–96
- [83] Nie X L, Wei S H and Zhang S B 2002 *Phys. Rev. B* **65** 075111
- [84] Hodby J W, Jenkins T E, Schwab C, Tamura H and Trivich D 1976 *J. Phys. C* **9** 1429–39
- [85] Raebiger H, Lany S and Zunger A 2007 *Phys. Rev. B* **76** 045209
- [86] Scanlon D O, Morgan B J, Watson G W and Walsh A 2009 *Phys. Rev. Lett.* **103** 096405
- [87] Wright A F and Nelson J S 2002 *J. Appl. Phys.* **92** 5849–51
- [88] Ameena F 2012 *PhD Thesis* The University of Texas, Arlington
- [89] Nolan M 2008 *Thin Solid Films* **516** 8130–5
- [90] Scanlon D O, Morgan B J and Watson G W 2009 *J. Chem. Phys.* **131** 124703
- [91] Rakhshani A E, Makdisi Y and Mathew X 1996 *Thin Solid Films* **288** 69–75
- [92] Paul G K, Nawa Y, Sato H, Sakurai T and Akimoto K 2006 *Appl. Phys. Lett.* **88** 141901
- [93] Paul G K, Ghosh R, Bera S K, Bandyopadhyay S, Sakurai T and Akimoto K 2008 *Chem. Phys. Lett.* **463** 117–20
- [94] Bose A, Basu S, Banerjee S and Chakravorty D 2005 *J. Appl. Phys.* **98** 074307
- [95] Kohler B U and Jansen M 1986 *Z. Anorg. Allg. Chem.* **543** 73–80
- [96] Trari M, Topfer J, Doumerc J P, Pouchard M, Ammar A and Hagenmuller P 1994 *J. Solid State Chem.* **111** 104–10
- [97] Shannon R D, Rogers D B and Prewitt C T 1971 *Inorg. Chem.* **10** 713
- [98] Ingram B J, Gonzalez G B, Mason T O, Shahriari D Y, Barnabe A, Ko D G and Poeppelmeier K R 2004 *Chem. Mater.* **16** 5616–22
- [99] Snure M and Tiwari A 2007 *Appl. Phys. Lett.* **91** 092123
- [100] Ruttanapun C 2013 *J. Appl. Phys.* **114** 113108
- [101] Kakehi Y, Satoh K, Yotsuya T, Masuko K, Yoshimura T, Ashida A and Fujimura N 2009 *J. Cryst. Growth* **311** 1117–22
- [102] Singh M, Singh V N and Mehta B R 2008 *J. Nanosci. Nanotechnol.* **8** 3889–94
- [103] Barnabe A, Thimont Y, Lalanne M, Presmanes L and Tailhades P 2015 *J. Mater. Chem. C* **3** 6012–24
- [104] Shin D, Foord J S, Egdel R G and Walsh A 2012 *J. Appl. Phys.* **112** 113718
- [105] Li X R, Han M J, Zhang X L, Shan C, Hu Z G, Zhu Z Q and Chu J H 2014 *Phys. Rev. B* **90** 035308
- [106] Han M J, Duan Z H, Zhang J Z, Zhang S, Li Y W, Hu Z G and Chu J H 2013 *J. Appl. Phys.* **114** 163526
- [107] Han M J, Jiang K, Zhang J Z, Yu W L, Li Y W, Hu Z G and Chu J H 2012 *J. Mater. Chem.* **22** 18463–70
- [108] Aston D J, Payne D J, Green A J H, Egdel R G, Law D S L, Guo J, Glans P A, Learmonth T and Smith K E 2005 *Phys. Rev. B* **72** 185115
- [109] Luo H M, Jain M, McCleskey T M, Bauer E, Burrell A K and Jia Q X 2007 *Adv. Mater.* **19** 3604
- [110] Nagarajan R, Duan N, Jayaraj M K, Li J, Vanaja K A, Yokochi A, Draeseke A, Tate J and Sleight A W 2001 *Int. J. Inorg. Mater.* **3** 265–70
- [111] Tate J, Ju H L, Moon J C, Zakutayev A, Richard A P, Russell J and McIntyre D H *Phys. Rev. B* **80** 165206
- [112] Ketir W, Saadi S and Trari M 2012 *J. Solid State Electrochem.* **16** 213–8
- [113] Scanlon D O and Watson G W 2010 *J. Phys. Chem. Lett.* **1** 3195–9
- [114] Scanlon D O and Watson G W 2011 *J. Mater. Chem.* **21** 3655–63
- [115] Scanlon D O, Godinho K G, Morgan B J and Watson G W 2010 *J. Chem. Phys.* **132** 024707
- [116] Scanlon D O, Walsh A and Watson G W 2009 *Chem. Mater.* **21** 4568–76
- [117] Scanlon D O, Walsh A, Morgan B J, Watson G W, Payne D J and Egdel R G 2009 *Phys. Rev. B* **79** 035101
- [118] Okuda T, Jufuku N, Hidaka S and Terada N 2005 *Phys. Rev. B* **72** 144403
- [119] Yokobori T *et al* 2013 *Phys. Rev. B* **87** 195124
- [120] Nie X L, Wei S H and Zhang S B 2002 *Phys. Rev. Lett.* **88** 066405
- [121] Singh M, Mehta B R, Varandani D and Singh V N 2009 *J. Appl. Phys.* **106** 093515
- [122] Pellicer-Porres J, Segura A, Gilliland A S, Munoz A, Rodriguez-Hernandez P, Kim D, Lee M S and Kim T Y 2006 *Appl. Phys. Lett.* **88** 181904

- [123] Katayama-Yoshida H, Koyanagi T, Funashima H, Harima H and Yanase A 2003 *Solid State Commun.* **126** 135–9
- [124] Hamada I and Katayama-Yoshida H 2006 *Physica B* **376** 808–11
- [125] Ingram B J, Harder B J, Hrabec N W and Mason T O 2004 *Chem. Mater.* **16** 5623–9
- [126] Ohta H, Orita M, Hirano M, Yagi I, Ueda K and Hosono H 2002 *J. Appl. Phys.* **91** 3074–8
- [127] Hu J P, Payne D J, Egdel R G, Harrison N M and Dhanak V R 2007 *Chem. Phys. Lett.* **450** 39–43
- [128] Lynch C C B, Egdel R G and Law D S L 2005 *Chem. Phys. Lett.* **401** 223–6
- [129] Godinho K G, Carey J J, Morgan B J, Scanlon D O and Watson G W 2010 *J. Mater. Chem.* **20** 1086–96
- [130] Godinho K G, Watson G W, Walsh A, Green A J H, Payne D J, Harmer J and Egdel R G 2008 *J. Mater. Chem.* **18** 2798–806
- [131] Kudo A, Yanagi H, Ueda K, Hosono H, Kawazoe H and Yano Y 1999 *Appl. Phys. Lett.* **75** 2851–53
- [132] Ohta H, Orita M, Hirano M and Hosono H 2001 *J. Appl. Phys.* **89** 5720–5
- [133] Ishikawa K, Kinoshita S, Suzuki Y, Matsuura S, Nakanishi T, Aizawa M and Suzuki Y 1991 *J. Electrochem. Soc.* **138** 1166–70
- [134] Palazzi M 1981 *C. R. Acad. Sci., Paris* **292** 789–91
- [135] Inoue S, Ueda K, Hosono H and Hamada N 2001 *Phys. Rev. B* **64** 245211
- [136] Imada M, Fujimori A and Tokura Y 1998 *Rev. Mod. Phys.* **70** 1039–263
- [137] Hiramatsu H, Ueda K, Ohta H, Orita M, Hirano M and Hosono H 2002 *Thin Solid Films* **411** 125–8
- [138] Hiramatsu H, Ueda K, Ohta H, Orita M, Hirano M and Hosono H 2002 *Appl. Phys. Lett.* **81** 598–600
- [139] Hosono H 2007 *Thin Solid Films* **515** 6000–14
- [140] Goto Y, Tanaki M, Okusa Y, Shibuya T, Yasuoka K, Matoba M and Kamihara Y 2014 *Appl. Phys. Lett.* **105** 022104
- [141] Ueda K, Hiramatsu H, Hirano M, Kamiya T and Hosono H 2006 *Thin Solid Films* **496** 8–15
- [142] Clarke S J, Adamson P, Herkelrath S J C, Rutt O J, Parker D R, Pitcher M J and Smura C F 2008 *Inorg. Chem.* **47** 8473–86
- [143] Ueda K and Hosono H 2002 *J. Appl. Phys.* **91** 4768–70
- [144] Hiramatsu H, Ueda K, Ohta H, Hirano M, Kikuchi M, Yanagi H, Kamiya T and Hosono H 2007 *Appl. Phys. Lett.* **91** 012104
- [145] Scanlon D O and Watson G W 2009 *Chem. Mater.* **21** 5435–42
- [146] Narushima S, Mizoguchi H, Shimizu K, Ueda K, Ohta H, Hirano M, Kamiya T and Hosono H 2003 *Adv. Mater.* **15** 1409–13
- [147] Mizoguchi H, Hirano M, Fujitsu S, Takeuchi T, Ueda K and Hosono H 2002 *Appl. Phys. Lett.* **80** 1207–9
- [148] Mansourian-Hadavi N, Wansom S, Perry N H, Nagaraja A R, Mason T O, Ye L H and Freeman A J 2010 *Phys. Rev. B* **81** 075112
- [149] Singh D J, Rai R C, Musfeldt J L, Auluck S, Singh N, Khalifah P, McClure S and Mandrus D G 2006 *Chem. Mater.* **18** 2696–700
- [150] Amini M N, Dixit H, Saniz R, Lamoén D and Partoens B 2014 *Phys. Chem. Chem. Phys.* **16** 2588–96
- [151] Scanlon D O and Watson G W 2011 *Phys. Chem. Chem. Phys.* **13** 9667–75
- [152] Kim T W, Woo M A, Regis M and Choi K S 2014 *J. Phys. Chem. Lett.* **5** 2370–4
- [153] Liu X J, Chang Z, Luo L, Xu T H, Lei X D, Liu J F and Sun X M 2014 *Chem. Mater.* **26** 1889–95
- [154] Wang S B, Ding Z X and Wang X C 2015 *Chem. Commun.* **51** 1517–9
- [155] Cheng J B, Lu Y, Qiu K W, Yan H L, Hou X Y, Xu J Y, Han L, Liu X M, Kim J K and Luo Y S 2015 *Phys. Chem. Chem. Phys.* **17** 17016–22
- [156] Sharma Y, Sharma N, Rao G V S and Chowdari B V R 2007 *Adv. Funct. Mater.* **17** 2855–61
- [157] Wu R B, Qian X K, Zhou K, Wei J, Lou J and Ajayan P M 2014 *ACS Nano* **8** 6297–303
- [158] Kim S, Cianfrone J A, Sadik P, Kim K W, Ivill M and Norton D P 2010 *J. Appl. Phys.* **107** 103538
- [159] Schein F L, Winter M, Bontgen T, von Wenckstern H and Grundmann M 2014 *Appl. Phys. Lett.* **104** 022104
- [160] Schlupp P, Schein F L, von Wenckstern H and Grundmann M 2015 *Adv. Electron. Mater.* **1** 5
- [161] Klupfel F J, Holtz A, Schein F L, von Wenckstern H and Grundmann M 2015 *IEEE Trans. Electron Devices* **62** 4004–8
- [162] Perkins J D *et al* 2011 *Phys. Rev. B* **84** 205207
- [163] Arca E, Fleischer K and Shvets I V 2011 *Appl. Phys. Lett.* **99** 3
- [164] Zhang K H L, Du Y G, Papadogianni A, Bierwagen O, Sallis S, Piper L F J, Bowden M E, Shutthanandan V, Sushko P V and Chambers S A 2015 *Adv. Mater.* **27** 5191–5
- [165] McClure D S 1963 *J. Chem. Phys.* **38** 2289
- [166] Lany S 2015 *J. Phys.: Condens. Matter* **27** 283203
- [167] Uekawa N and Kaneko K 1996 *J. Phys. Chem.* **100** 4193–8
- [168] Norton E, Farrell L, Callaghan S D, McGuinness C, Shvets I V and Fleischer K 2016 *Phys. Rev. B* **93** 115302
- [169] Farrell L, Fleischer K, Caffrey D, Mullarkey D, Norton E and Shvets I V 2015 *Phys. Rev. B* **91** 125202
- [170] Sushko P V, Qiao L, Bowden M, Varga T, Exarhos G J, Urban F K, Barton D and Chambers S A 2013 *Phys. Rev. Lett.* **110** 077401
- [171] Zhang K H L, Du Y, Sushko P V, Bowden M E, Shutthanandan V, Sallis S, Piper L F J and Chambers S A 2015 *Phys. Rev. B* **91** 155129
- [172] Chambers S A, Qiao L, Droubay T C, Kaspar T C, Arey B W and Sushko P V 2011 *Phys. Rev. Lett.* **107** 206802
- [173] Walsh A, Payne D J, Egdel R G and Watson G W 2011 *Chem. Soc. Rev.* **40** 4455–63
- [174] Walsh A and Watson G W 2005 *J. Solid State Chem.* **178** 1422–8
- [175] Walsh A and Watson G W 2004 *Phys. Rev. B* **70** 235114
- [176] Ogo Y, Hiramatsu H, Nomura K, Yanagi H, Kamiya T, Kimura M, Hirano M and Hosono H 2009 *Phys. Status Solidi a* **206** 2187–91
- [177] Liang L Y, Cao H T, Chen X B, Liu Z M, Zhuge F, Luo H, Li J, Lu Y C and Lu W 2012 *Appl. Phys. Lett.* **100** 263502
- [178] Fortunato E, Barros R, Barquinha P, Figueiredo V, Park S H K, Hwang C S and Martins R 2010 *Appl. Phys. Lett.* **97** 052105
- [179] Yabuta H, Kaji N, Hayashi R, Kumomi H, Nomura K, Kamiya T, Hirano M and Hosono H 2010 *Appl. Phys. Lett.* **97** 072111
- [180] Quackenbush N F *et al* 2013 *Chem. Mater.* **25** 3114–23
- [181] Varley J B, Schleife A, Janotti A and Van de Walle C G 2013 *Appl. Phys. Lett.* **103** 082118
- [182] Hosono H, Ogo Y, Yanagi H and Kamiya T 2011 *Electrochem. Solid State Lett.* **14** H13–6
- [183] Jain A, Ong S P, Hautier G, Chen W, Richards W D, Dacek S, Cholia S, Gunter D, Skinner D, Ceder G and Persson K A 2013 *APL Mater.* **1** 11
- [184] Sawatzky G A and Allen J W 1984 *Phys. Rev. Lett.* **53** 2339–42
- [185] Sato H, Minami T, Takata S and Yamada T 1993 *Thin Solid Films* **236** 27–31

- [186] Vanelp J, Eskes H, Kuiper P and Sawatzky G A 1992 *Phys. Rev. B* **45** 1612–22
- [187] Goodenough J B, Wickham D G and Croft W J 1958 *J. Phys. Chem. Solids* **5** 107–16
- [188] Dutta T, Gupta P, Gupta A and Narayan J 2010 *J. Appl. Phys.* **108** 073708
- [189] Kuiper P, Kruizinga G, Ghijsen J, Sawatzky G A and Verweij H 1989 *Phys. Rev. Lett.* **62** 221–4
- [190] Pickering I J, George G N, Lewandowski J T and Jacobson A J 1993 *J. Am. Chem. Soc.* **115** 4137–44
- [191] Antolini E 2003 *Mater. Chem. Phys.* **82** 937–48
- [192] Bosman A J and Crevecoeur C 1966 *Phys. Rev.* **144** 763
- [193] Chen S C, We C K, Kuo T Y, Peng W C and Lin H C 2014 *Thin Solid Films* **572** 51–5
- [194] Gupta R K, Ghosh K and Kahol P K 2009 *Physica E* **41** 617–20
- [195] Ohta H, Hirano M, Nakahara K, Maruta H, Tanabe T, Kamiya M, Kamiya T and Hosono H 2003 *Appl. Phys. Lett.* **83** 1029–31
- [196] Lee W Y, Mauri D and Hwang C 1998 *Appl. Phys. Lett.* **72** 1584–6
- [197] Ohta H, Kamiya M, Kamaiya T, Hirano M and Hosono H 2003 *Thin Solid Films* **445** 317–21
- [198] Niklasson G A and Granqvist C G 2007 *J. Mater. Chem.* **17** 127–56
- [199] Xia X H, Tu J P, Zhang J, Wang X L, Zhang W K and Huang H 2008 *Sol. Energy Mater. Sol. Cells* **92** 628–33
- [200] Son J Y and Shin Y H 2008 *Appl. Phys. Lett.* **92** 2106
- [201] Lee M J *et al* 2009 *Nano Lett.* **9** 1476–81
- [202] He J J, Lindstrom H, Hagfeldt A and Lindquist S E 1999 *J. Phys. Chem. B* **103** 8940–3
- [203] Irwin M D, Buchholz B, Hains A W, Chang R P H and Marks T J 2008 *Proc. Natl Acad. Sci. USA* **105** 2783–7
- [204] Yan F, Zhang X W, Yu Y G, Yu L P, Nagaraja A, Mason T O and Zunger A 2015 *Nat. Commun.* **6** 7308
- [205] Zhang L *et al* 2016 *Nat. Mater.* **15** 204–10